

A New Crater Near InSight: Implications for Seismic Impact Detectability on Mars

Authors:

I. J. Daubar, Department of Earth, Environmental, and Planetary Sciences, Brown University, Campus Box 1846, Providence, RI 02912-1846, USA. *Corresponding author.*

Ingrid_daubar@brown.edu

P. Lognonné, Université de Paris, Institut de physique du globe de Paris, CNRS, F-75005 Paris, France

N. A. Teanby, School of Earth Sciences, University of Bristol, Wills Memorial Building, Queens Road, Bristol BS8 1RJ, UK

G. S. Collins, Department of Earth Science and Engineering, Imperial College London, South Kensington Campus, London SW7 2AZ, UK

J. Clinton, Swiss Seismological Service (SED), ETH Zurich, Sonneggstr. 5, 8092 Zurich, Switzerland

S. Stähler, Institute of Geophysics, ETH Zürich, Sonneggstrasse 5, 8092 Zürich, Switzerland

A. Spiga, Laboratoire de Météorologie Dynamique / Institut Pierre Simon Laplace (LMD/IPSL), Sorbonne Université, Centre National de la Recherche Scientifique (CNRS), École Polytechnique, École Normale Supérieure (ENS), Campus Pierre et Marie Curie BC99, 4 place Jussieu, 75005 Paris, France

F. Karakostas, University of Maryland, College Park, Department of Geology, 8000 Regents Dr., College Park, MD, 20782-4211, USA

S. Ceylan, Institute of Geophysics, ETH Zurich, Sonneggstr. 5, 8092 Zurich, Switzerland

M. Malin, Malin Space Science Systems, San Diego, CA

A. S. McEwen, University of Arizona, Tucson, AZ

R. Maguire, University of Maryland, College Park, Department of Geology, 8000 Regents Dr., College Park, MD, 20782-4211, USA

C. Charalambous, Department of Electrical and Electronic Engineering, Imperial College London, South Kensington Campus, London, SW7 2AZ, United Kingdom

K. Onodera, Université de Paris, Institut de physique du globe de Paris, CNRS, F-75005 Paris, France

A. Lucas, Université de Paris, Institut de physique du globe de Paris, CNRS, F-75005 Paris, France

L. Rolland, Université Côte d'Azur, Observatoire de la Côte d'Azur, CNRS, IRD, Géoazur, 250 av Einstein, 06560, Valbonne, France

J. Vaubaillon, Observatoire de Paris, IMCCE, PSL, 77 Av Denfert Rochereau, 75014 Paris, France

T. Kawamura, Université de Paris, Institut de physique du globe de Paris, CNRS, F-75005 Paris, France

M. Böse, Swiss Seismological Service (SED), ETH Zurich, Sonneggstr. 5, 8092 Zurich, Switzerland

A. Horleston, School of Earth Sciences, University of Bristol, Wills Memorial Building, Queens Road, Bristol BS8 1RJ, UK

44 M. van Driel, Institute of Geophysics, ETH Zurich, Sonneggstr. 5, 8092 Zurich, Switzerland
45 J. Stevanović, AWE Blacknest, Aldermaston, Reading, GR7 4RS, UK
46 K. Miljković, Space Science and Technology Centre, School of Earth and Planetary Sciences,
47 Curtin University, GPO Box U1987, Perth, WA 6845, Australia
48 B. Fernando, Department of Earth Sciences, University of Oxford, South Parks Road, Oxford
49 OX1 3AN, United Kingdom
50 Q. Huang, Department of Geology, University of Maryland, College Park, 8000 Regents Dr.,
51 College Park, MD, 20782-4211, USA
52 D. Giardini, Institute of Geophysics, ETH Zurich, Sonneggstr. 5, 8092 Zurich, Switzerland
53 C. S. Larmat, Los Alamos National Laboratory, PO Box 1663, Los Alamos, NM 87545, USA
54 K. Leng, Department of Earth Sciences, University of Oxford, South Parks Road, Oxford OX1
55 3AN, UK
56 A. Rajšić, Space Science and Technology Centre, School of Earth and Planetary Sciences, Curtin
57 University, GPO Box U1987, Perth, WA 6845, Australia
58 N. Schmerr, University of Maryland, College Park, Department of Geology, 8000 Regents Dr.,
59 College Park, MD, 20782-4211, USA
60 N. Wójcicka, Department of Earth Science and Engineering, Imperial College London, South
61 Kensington Campus, London SW7 2AZ, UK
62 T. Pike, Department of Electrical and Electronic Engineering, Imperial College London, South
63 Kensington Campus, London, SW7 2AZ, United Kingdom
64 J. Wookey, School of Earth Sciences, University of Bristol, Wills Memorial Building, Queens
65 Road, Bristol BS8 1RJ, UK
66 S. Rodriguez, Université de Paris, Institut de physique du globe de Paris, CNRS, F-75005 Paris,
67 France
68 R. Garcia, Institut Supérieur de l'Aéronautique et de l'Espace SUPAERO, 10 Avenue Edouard
69 Belin, 31400 Toulouse, France
70 M. E. Banks, NASA Goddard Space Flight Center, 8800 Greenbelt Road, Greenbelt, MD 20771,
71 USA
72 L. Margerin, Institut de Recherche en Astrophysique et Planétologie, Université Toulouse III
73 Paul Sabatier, CNRS, CNES, 14 Av. E. Belin, 31400, Toulouse, France
74 L. Posiolova, Malin Space Science Systems, San Diego, CA
75 B. Banerdt, Jet Propulsion Laboratory, California Institute of Technology, Pasadena, CA 91109,
76 USA
77

78 **Key Points**

- 79
- 80 • A new 1.5 m diameter impact crater formed on Mars ~40 km from the InSight lander
81 between February and April 2019.
 - 82 • Three candidate seismic events occurred during this time frame, but none of them can be
83 definitively associated with the new crater.
 - 84 • We revise our expectations for InSight impact detections above the background noise to
85 be ~2 per Earth year, with large uncertainties.
- 86
87

88 **Index terms:**

89 5420 PLANETARY SCIENCES: SOLID SURFACE PLANETS - Impact phenomena, cratering
90 (6022, 8136)

91 7299 SEISMOLOGY - General or miscellaneous

92 8136 TECTONOPHYSICS - Impact phenomena (5420, 6022)

93

94

95 **Abstract**

96

97 A new 1.5 meter diameter impact crater was discovered on Mars only ~40 km from the
98 InSight lander. Context camera images constrained its formation between February 21 and April
99 6, 2019; follow-up HiRISE images resolved the crater. During this time period, three seismic
100 events were identified in InSight data. We derive expected seismic signal characteristics and use
101 them to evaluate each of the seismic events. However, none of them can definitively be
102 associated with this source. Atmospheric perturbations are generally expected to be generated
103 during impacts; however, in this case, no signal could be identified as related to the known
104 impact. Using scaling relationships based on the terrestrial and lunar analogs and numerical
105 modeling, we predict the amplitude, peak frequency, and duration of the seismic signal that
106 would have emanated from this impact. The predicted amplitude falls near the lowest levels of
107 the measured seismometer noise for the predicted frequency. Hence it is not surprising this
108 impact event was not positively identified in the seismic data. Finding this crater was a lucky
109 event as its formation this close to InSight has a probability of only ~0.2, and the odds of
110 capturing it in before and after images is extremely low. We revisit impact-seismic
111 discriminators in light of real experience with a seismometer on the martian surface. Using
112 measured noise of the instrument, we revise our previous prediction of seismic impact detections
113 downwards, from ~a few to tens, to just ~2 per Earth year, still with an order of magnitude
114 uncertainty.

115

116 **Plain Language Summary**

117

118 A small new impact crater was discovered on Mars very close to the InSight lander. Photographs
119 from a camera in orbit show it formed between February 21 and April 6, 2019. Three seismic
120 events were detected by InSight during this time. We estimate what seismic data from the impact
121 would have looked like and whether or not each of the seismic events was caused by the new
122 impact, but none of them can be definitely linked. We predict the size, frequency, and length of
123 time of the signal that would have come from this impact. Even though this impact is very close
124 to InSight, it's small, so it was not a large seismic event. The signal would be near the quietest
125 the instrument ever gets. There is only a 1 in 5 chance per Earth year that a crater would have
126 formed this close to InSight, and a much lower chance that it would be imaged, thus we were
127 very lucky to find this crater. Using what we know about the instrument on the ground, we
128 update the number of impacts we expect to find with InSight to ~2 each Earth year, with a lot of
129 uncertainty.

130

131

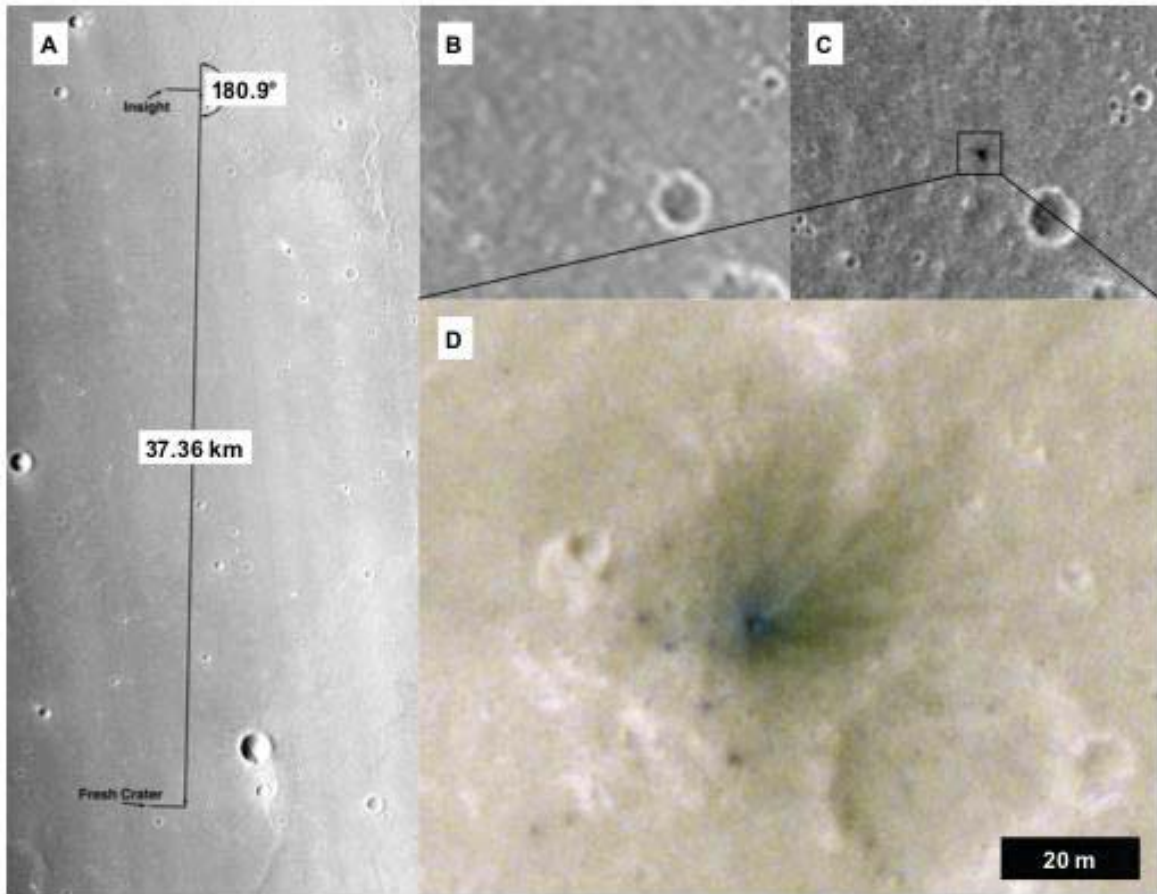
132 **1 A new impact constrained by orbital images**

133
134 On April 6, 2019, an image taken by the Context camera (CTX; Malin *et al.*, 2007) on the
135 Mars Reconnaissance Orbiter (MRO) revealed a new dark spot that was not present in a previous
136 image taken on February 21 (Fig. 1), only ~40 km from the newly-landed InSight mission
137 (Interior Exploration using Seismic Investigations, Geodesy and Heat Transport; Smrekar *et al.*,
138 2019). Detecting an impact in both seismic data and orbital images would be an exciting
139 development, leading to a number of scientific advances (Daubar *et al.*, 2018). This would be a
140 seismic source with a known location, and thus a known distance and direction. A certain
141 location and depth would allow modeling of seismic ray paths through the interior that could
142 constrain seismic velocities and the physical properties of the material through which the rays
143 traveled. This would improve models of interior structure and the seismic attenuation of Mars.
144 An impact clearly observed in both orbital and seismic data would also provide a calibration of
145 the seismic source parameters such as moment, cutoff frequency, and seismic efficiency (the
146 ratio of impact energy to radiated seismic energy). The seismic efficiency, for example, is not
147 well constrained, with values in the literature ranging from 10^{-6} to 10^{-2} (Daubar *et al.*, 2018 and
148 references therein). High resolution images of newly formed craters would characterize crater
149 sizes, leading to an empirical relationship between impact size and observed seismic amplitudes.
150 Enough such observations would also result in an independent measurement of the current
151 impact rate, anchoring absolute bombardment rates. Thus identifying an impact in seismic data
152 that was also imaged from orbit would satisfy many important scientific goals. So naturally, this
153 event was of immediate interest to the InSight team.

154
155 A high-resolution 25 cm pixel scale image from the High Resolution Imaging Science
156 Experiment (HiRISE; McEwen *et al.*, 2007) was acquired shortly thereafter. The HiRISE image
157 resolved a ~1.5 meter diameter impact crater at the location of the new dark spot (Fig. 1D),
158 showing that an impact event occurred in the short period of time constrained by the before and
159 after CTX images, between 21 February (03:56:17 UTC) and 6 April (08:19:17 UTC) in 2019.
160 This occurrence is not especially rare; ~900 new dated impacts have been discovered in the last
161 ~decade on Mars using similar techniques (Malin *et al.*, 2007; Daubar *et al.*, 2013), although the
162 imaging date constraints are usually on the order of a few years rather than a month. This impact
163 was also extraordinary in its location very close to the recently-landed InSight mission. At this
164 distance, the prospect of detecting the impact event using the seismic and atmospheric
165 instrumentation on InSight was an exciting possibility. This is the only impact we know to have
166 formed this close to the lander during the time since InSight landed on Mars on 26 November
167 2018.

168
169 The new crater is located at 3.866°N planetocentric latitude, 135.613°E longitude, just
170 37.36 km from InSight, which landed at 4.502°N, 135.623°E (Parker *et al.*, 2019). It is located
171 along an azimuth of 180.9°, almost directly south of the lander. The asymmetric low-albedo blast
172 zone pattern around the crater (Fig. 1D), caused by the disturbance of light-toned dust during the
173 impact, indicates a somewhat oblique impact coming from the southwest direction. Small dark
174 spots to the southwest of the crater could be blast zones around secondary craters or multiple
175 smaller primary craters in a clustered impact that formed when the impactor fragmented in the
176 atmosphere (Daubar *et al.*, 2019). Craters within these smaller dark spots are not resolved. The
177 pattern of dark spots is more consistent with a clustered impact than with secondary craters;

178 secondary craters would be concentrated downrange rather than uprange, and typically have
 179 more symmetric radial patterns. In either case, the contribution of the group of smaller craters to
 180 a combined seismic signal would be negligible compared with that of the main ~1.5 m diameter
 181 crater (Schmerr *et al.*, 2019).
 182
 183
 184



185
 186 Figure 1.
 187 *New crater observations. (A) CTX context image showing locations of InSight lander and new*
 188 *dated impact. (B) CTX image K14_068929_1845_XN_04N224W_190221 taken February 21,*
 189 *2019 (6 m/px). (C) CTX image K16_059495_1829_XN_02N224W_190406 taken April 6, 2019,*
 190 *showing new dark spot that was not present in previous image. (D) Cutout from HiRISE image*
 191 *ESP_060128_1840 (COLOR RDR; 25 cm/px) showing new impact crater. North is up, and*
 192 *images have been stretched for contrast. Image credits: NASA/JPL/MSSS (CTX);*
 193 *NASA/JPL/University of Arizona (HiRISE).*
 194

195 A second HiRISE image was acquired to obtain stereo data, but the crater is not resolved
 196 in the resulting Digital Terrain Model (DTM). (See anaglyph in Fig. S1.) A depth of a few tens

197 of centimeters is estimated for the new crater. Although this depth is not resolved in the DTM, an
198 estimate was possible by scaling from larger, resolved, craters in the DTM.

199
200 In subsequent sections we derive the expected seismic and atmospheric signals that
201 would have been produced by this known impact and have the potential to have been detected by
202 InSight (Section 2). In Section 3, we describe the search of the seismic data during the time
203 period constrained by the before and after CTX images, and the three candidate seismic events
204 that were found. We then evaluate which of those seismic events, and any associated
205 atmospheric signals, might be connected with the formation of the new crater. Finally, in Section
206 4, we use InSight mission experience thus far to re-evaluate the seismic impact discriminators we
207 identified before landing, and we present updated expectations for impact detections with InSight
208 in light of real data acquired since landing.

210 **2 Predicted signals from the new impact crater**

211 2.1 Predicted impact parameters from the observed crater

212
213 To assess the detectability of the observed ~1.5 m diameter crater by InSight, we first
214 estimate the impactor parameters. The geology of the impact target area is very similar to that in
215 the immediate vicinity of the InSight lander, which has been characterized in detail (Golombek
216 *et al.*, 2020). The material in which the crater formed is likely to be a loose, porous regolith with
217 very low cohesive strength ($\lesssim 50$ kPa). The diameter of meter-scale impact craters formed in
218 such a material is expected to scale as a power of the vertical impactor momentum, with only
219 minor additional dependence on other impactor parameters (Holsapple, 1993; Holsapple and
220 Housen, 2007). For a 1.5 ± 0.25 m diameter crater, the predicted vertical impactor momentum is
221 100-3000 Ns, depending on the cohesive strength of the regolith (Fig. S2). The lower limit
222 applies if the martian regolith can be represented as cohesionless dry sand; a nominal upper limit
223 applies if the martian regolith has an effective cohesive strength of 50 kPa. An even higher
224 impactor momentum is possible, but that would require a cohesive strength of a well-cemented
225 terrestrial soil, which is not compatible with observations of the martian regolith made in the
226 vicinity of the InSight lander (Golombek *et al.*, 2020).

227
228 The seismic source of the impact can be expressed as an equivalent seismic moment,
229 which scales approximately linearly with impactor momentum according to two independently
230 derived, semi-empirical scaling relationships (Shishkin, 2007; Gudkova *et al.* 2011, 2015;
231 reviewed in Daubar *et al.*, 2018). For an impactor momentum of 100-3000 Ns, these
232 relationships predict an equivalent seismic moment of 10^6 - 10^7 Nm (Fig. S3).

233
234 The estimated impactor momentum implies an impactor mass ~0.1 to ~1 kg, depending
235 on impact speed. Meteoroids in this mass range are substantially decelerated by Mars'
236 atmosphere (Fig. S4) and are predicted to lose approximately 90% of their initial kinetic energy,
237 75% of their initial speed, and 30% of their initial mass by ablation and drag before striking the
238 ground (Table S1). Thus vertical impact speeds at the ground in the range of only 1-3 km/s are
239 expected for typical pre-entry meteoroid encounter speeds of 5-15 km/s (Le Feuvre and
240 Wicczorek, 2008; JeongAhn and Malhotra, 2015) and entry angles of 15-90°. At these relatively

241 slow impact speeds, and taking into account the uncertainty in impactor momentum, estimates of
242 the impact energy range from approximately 0.1 MJ to 2 MJ (see supplemental section S1).

243
244 An independent test of these energy estimates is provided by the empirical relationship
245 from Teanby and Wookey (2011) between crater diameter (D) and impact energy (E), based on
246 laboratory and field impact experiments, explosive analogues, and the Apollo artificial lunar
247 impacts:

$$248 \quad D = 8.8_{-3.5}^{+2.6} \times 10^{-3} E^{0.32 \pm 0.01} \left(\frac{g_{\oplus}}{g} \right)^{3/16}, \quad (1)$$

249
250 where g_{\oplus} is Earth's gravity (9.81 ms^{-2}) and g is Mars' gravity (3.73 ms^{-2}). The error bars
251 incorporate scatter in the source data and the uncertainties in impact conditions. Using this
252 relationship gives an estimated ground impact energy of 5.3 ± 1.8 MJ, which is somewhat larger
253 than our previous estimate. We attribute this difference to the fact that most of the data used to
254 construct Eq. (1) are from experiments in terrestrial soils and rocks that have a much higher
255 cohesive strength than the strength we adopt for the martian regolith based on in situ and remote
256 sensing of this region. Therefore, this scaling relationship provides an upper bound on the impact
257 energy.

258
259

2.2 Predicted seismic signals based on energy and moment scaling

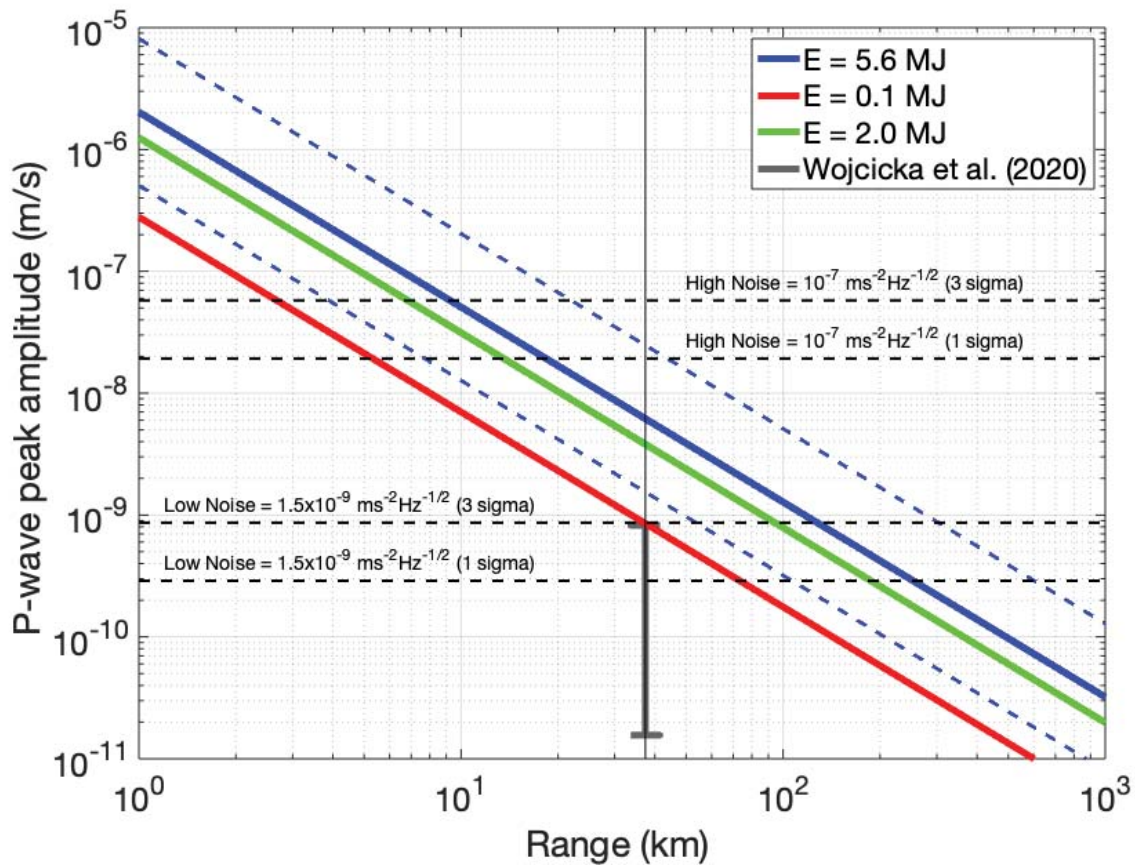
260
261
262 The estimated ground impact energy can be used to obtain a first order prediction of
263 seismic P-wave amplitude v at source-receiver distance x using scaling relations developed for
264 terrestrial impacts (Teanby, 2015):

$$265 \quad v(x, E) = ax^b E^c \quad (2)$$

266
267
268 where scaling law constants $a=5.6 \times 10^{-5}$, $b=-1.6$, and $c=0.5$ under Mars conditions (Teanby,
269 2015). The overall uncertainty on $v(x, E)$ is a factor of four. This relationship is strictly only
270 valid over the range of energies and distances used by Teanby (2015), which cover ~ 400 - $10,000$
271 kg TNT equivalent ($\sim 2 \times 10^3$ - 4×10^4 MJ) (excluding the very high energy buried nuclear
272 explosions) and 0.5-1200 km ranges. These events had peak seismic frequencies in the range 1-
273 16 Hz, with the Apollo lunar and Carancas Earth impacts peaking from 1-10 Hz. We can also
274 estimate the longest timescale in the source function using crater excavation timescale, $\tau = \sqrt{D/g}$
275 ~ 0.6 s, implying a frequency content of >1 Hz. Therefore, the scaling relationship is a
276 reasonable, although not ideal, match to conditions for the new martian crater, with the P-wave
277 frequency content likely peaking at a few Hz or slightly higher.

278
279 A first order prediction of seismic P-wave amplitude v for the new event is shown in
280 Figure 2 compared to the range of measured InSight noise levels in the 1-16 Hz bandpass from
281 Lognonné *et al.* (2019, 2020). The estimated P-wave amplitude at the observed range of 37 km is
282 0.8 - $4 \times 10^{-9} \text{ ms}^{-1}$ for 0.1-2.0 MJ and $6 \times 10^{-9} \text{ ms}^{-1}$ with a factor of four uncertainty for the 5.6 MJ
283 upper bound. Furthermore, Wójcicka *et al.* (2020) use numerical impact simulations to propose a
284 recasting of the amplitude scaling in terms of impact momentum instead of energy, which relates

285 to seismic moment more closely to linearly. When applied to impacts in relevant analog
 286 materials, this recasting results in a reduction in predicted seismic amplitudes by up to two orders
 287 of magnitude for small craters. Overall, these scaling laws have large uncertainties, and
 288 predictions span three orders of magnitude, but all imply a modest signal-to-noise ratio (SNR),
 289 with a likely SNR of only ~ 1 on average. These amplitude estimates are also in reasonable
 290 agreement with peak ground velocities predicted from numerical waveform simulations of the
 291 impact event (see supplemental section S2). During the detection period, the continuous
 292 seismometer data coverage is limited to 10 sps (5 Hz Nyquist) sampling except during
 293 exceptional periods where 20 sps or 100 sps was collected (Fig. S10). Therefore, any seismic
 294 energy over 5 Hz is unlikely to have been recorded for the majority of the time in question. The
 295 combination of low SNR, high frequency content, and low sample rate implies this event would
 296 have been be very difficult to detect seismically.
 297
 298



299

300 Figure 2.

301 *Estimated amplitude of P-wave signal from the 1.5 m diameter new impact. The amplitude is*
 302 *estimated using the impact energy scaling relationship from Teanby (2015) in equation (2) as*
 303 *described in the text. Solid lines show nominal amplitude prediction from scaling relations and*
 304 *uncertainty for three potential impact energies, a nominal range (red to green) and an upper*
 305 *limit (blue). Dashed blue lines show uncertainty on the upper limit $E=5.6$ MJ case. Horizontal*

306 dashed lines show range of seismic noise measured at 4 Hz at the InSight landing site for 1 and 3
 307 sigma (Lognonné et al., 2019, 2020), and vertical black line shows the distance between InSight
 308 and the new crater. Gray vertical bar shows range of predictions from Wójcicka et al. (2020)
 309 from numerically derived impact momentum scaling. Seismic noise amplitudes are converted to
 310 equivalent velocities by integrating the amplitude spectral density (ASD) noise for the 1-16 Hz
 311 bandwidth, using equation 14 in Teanby (2015). Amplitude estimates for the observed impact are
 312 at or below the noise levels.
 313

314 2.3 Predicted seismic signals based on lunar impact analogies

315
 316 The closest seismic analog for this impact is the Lunar Module of Apollo 14 (LM), which
 317 impacted 67 km from the Apollo Lunar Surface Experiments Package (ALSEP) station of Apollo
 318 14. Its amplitude was about 40 data units (DU) on the vertical Long Period (LP) axis in peaked
 319 mode, corresponding to 2 nm of ground displacement at 2 sec. See Lognonné et al. (2009) for a
 320 detailed analysis of this and other lunar impacts.
 321

322 At such a small epicentral distance, intrinsic attenuation can be neglected, and the seismic
 323 signal is mostly constrained by the elastic propagation properties, which are mostly diffusive on
 324 the Moon, and the source parameters. These parameters are summarized in Table 1.
 325
 326

Impact	Distance from seismometer (km)	Velocity (km/s)	Angle (° from vertical)	Mass (kg)	Mv (Mv _z) (kg m/s)	Rim Diam (m)	Depth (m)	Formation time
LM impact on the Moon	67	1.68	86.4°	2383	4×10 ⁶ (2.5×10 ⁵)	6.5	1.37	0.94 sec
New 1.5-m crater on Mars	37.4	1-3	Not well constrained; moderately oblique	0.1-1	1.4 ×10 ² - 4.3 ×10 ³ (1×10 ² - 3×10 ³)	1.5	A few tens of cm	~0.30- 0.35 sec

327

328 Table 1.

329 Comparison between the source parameters of the Apollo 14 Lunar Module (LM) impact and the
 330 CTX-image-constrained impact that formed the new 1.5-m diameter crater discussed in this
 331 paper. Parameters from the LM impacts are from Lognonné et al. (2009) and references therein.
 332 A 45° impact angle is assumed for the martian impact, although this is only weakly constrained.
 333 Formation time is estimated from Holsapple (1993) and using $0.5\sqrt{D/g}$ as an estimate of the

334 crater growth time (Schmidt and Housen, 1987). Known values are given in bold, other values
335 are inferred.

336
337
338
339

According to Sato and Korn (2007), the maximum amplitude of a pulse propagating in
340 the multiple forward scattering regime is proportional to $\sqrt{\frac{1}{xT_m}}$, where x is the hypocentral
341 distance and T_m is a characteristic time scale. T_m depends on the heterogeneity of the medium as:

$$342 \quad T_m = \sqrt{\pi} \frac{\langle \varepsilon^2 \rangle D^2}{2\alpha\beta} \quad (3)$$

343 Where β is the wave propagation speed, α is the correlation length of the random fluctuations,
344 and their variance is $\langle \varepsilon^2 \rangle$. This theory predicts that the typical maximum amplitude is

345 proportional to $\sqrt{\frac{\alpha\beta}{x^3 \langle \varepsilon^2 \rangle}}$. Note these formulae are valid in media with velocity and density with
346 gaussian fluctuations (Sato and Korn, 2007).

347

348 We do not expect the correlation distance to differ significantly between Mars and the
349 Moon, but fluctuations are certainly stronger on the Moon because scattering is stronger. As the
350 diffusivity is inversely proportional to $\langle \varepsilon^2 \rangle$, we expect the amplitude to be 5 to 10 times larger
351 on Mars than on the Moon, for the same source and distance, following initial comparisons of the
352 crustal diffusivity (Lognonné *et al.*, 2020).

353

354 With these assumptions, we can convert amplitudes of impacts detected on the Moon to
355 the martian situation. Following previous work (Lognonné *et al.*, 2009; Gudkova *et al.*, 2011;
356 2015), we assume that the amplitude of the signal is linearly related to the vertical momentum,
357 which implies a source for the martian impact smaller in moment than the LM source by a factor
358 of ~83-2500. On the other hand, the difference in diffusion makes the maximum amplitude of
359 the signal larger by a factor 5-10. Last but not least, the difference in distance for the LM impact
360 at 67 km makes the signal larger by a factor of 2.37 for an -1.5 exponential decay, comparable to
361 the -1.6 power law decay of local magnitudes on Earth at short distance (Richter, 1958).
362 Combining these factors, this suggests a martian signal smaller than the lunar one by a factor of
363 8.3-500 without a geometrical spreading correction; with that correction, it would be smaller by a
364 factor of 3.5-210.

365

366 The duration of the signal can also be addressed with similar analogies. Martian signals
367 are expected to have much shorter durations than lunar ones due to the ratio of diffusivities. Rise
368 times are found to be in the range of 600-800 sec for lunar impacts (Gillet *et al.*, 2017) and are
369 expected to be reduced by a factor of 30-100 for Mars. Signals with SNR of 3 will have
370 durations of about 2-3 times the rise time, leading to durations in the range of 20-60 seconds for
371 each phase in this case.

372

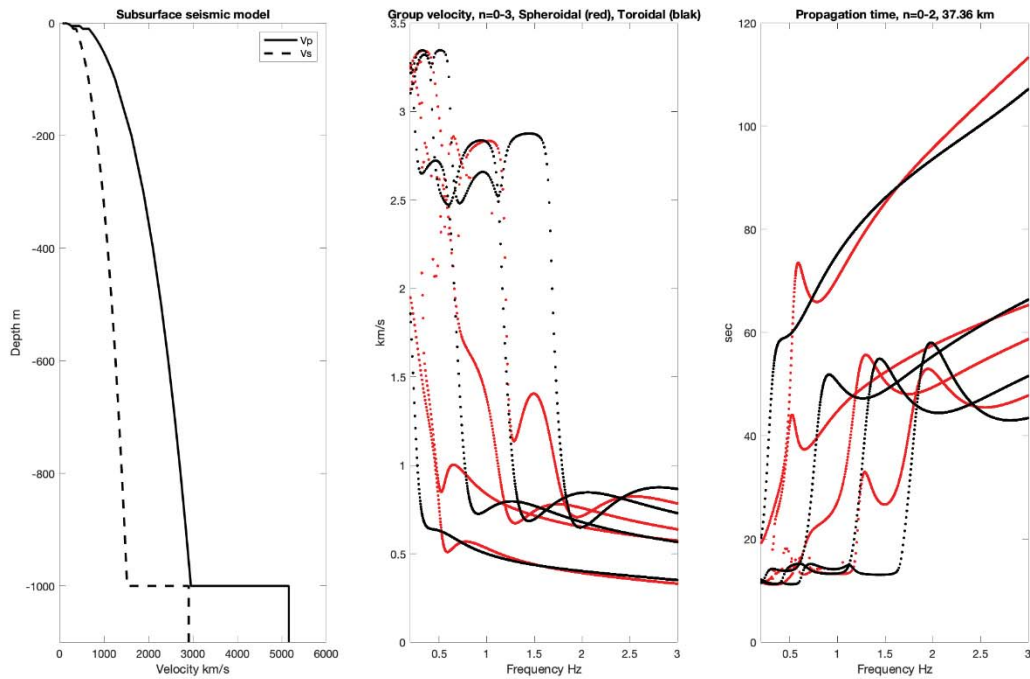
373

374 In summary, based on early estimates of the diffusivity of Mars, we expect this impact on
375 Mars to have a signal smaller in amplitude by a factor of 3.5 to 210 compared to the Apollo 14

376 LM impact recorded by the Apollo 12 vertical LP instrument. Martian impact signals are also
377 expected to have much shorter durations of ~20-60 seconds.
378

379 In order to estimate propagation time differences between the main phases, we use the
380 fact that an event at a distance of 37 km in a homogenous martian crust will propagate down to a
381 depth of ~500 m. We can expect that most of the energy of this event will therefore be guided in
382 the first half km of depth, for which seismic velocities are expected up to 2000 m/s for P waves
383 and 1000 m/s for S waves. Most of the energy will be in surface waves, for which typical group
384 velocities are computed with Mineos software (<https://geodynamics.org/cig/software/mineos/>)
385 (Fig. 3a). These are shown for one possible model of the shallow subsurface structure based on
386 constraints proposed by Lognonné *et al.* (2020) for the first five meters of depth, measurements
387 of the seismic velocities of layers of volcanic material (Lesage *et al.*, 2018) down to 1 km depth,
388 and the TAYAK reference model below that (Smrekar *et al.*, 2019). See supplemental section S3
389 for details of the model. Note that apart from the first five meters, this model is merely
390 representative, constrained only by earth analog. Propagation times (Fig. 3b) range from 11-15
391 sec to 80 sec for the four first spheroidal/toroidal surface wave branches. We note that the ratio
392 between the fundamental and the harmonic group velocities can be much larger than the standard
393 $\sqrt{3}$ ratio between the velocities of P and S body waves used by MQS (see Section 3). As an
394 example, the 78 seconds between the two phases of event S0116a (discussed in section 3.1) are
395 compatible with a slow packet propagating at 360 m/s (roughly the shear wave velocity at the
396 base of the bedrock in our model) and a second packet propagating four times faster, which is
397 roughly the P-wave velocity at a depth of ~100 meters, as proposed by Lesage *et al.* (2018). A
398 difference of several minutes between the arrival of the first and second pulse is also found in
399 event S0105a (see section 3.1). Second arrivals such as these might also be fundamental
400 scattered Rayleigh waves, while the first arrivals could be overtones propagating in the deeper
401 bedrock. The group velocity of the subsurface models also shows a clear variation of the group
402 velocity just above 0.5 Hz, which might be the reason the signal has a cutoff frequency ~0.5 Hz.

403
404



405

406 Figure 3.

407 (Left) Subsurface seismic model. (Middle) Group velocities of the fundamental Rayleigh and
 408 Love waves and of the three first spheroidal (red) and toroidal (black) overtones. (Right)
 409 Propagation time of the surface wave packet to a distance of 37.36 km, as a function of
 410 frequency up to 3 Hz. Model data is provided in Table S2.

411

412 In summary, based on lunar data extrapolated to Mars, the shallow layers and diffusivity
 413 of Mars suggests that for an event at the distance of the new crater, we expect phase durations of
 414 30 sec to 1 minute, with differences in phase arrivals up to about one minute.

415

416 2.4 Predicted atmospheric signals

417

418 A meteor entering the atmosphere and causing an impact crater would generate at various
 419 atmospheric levels in the entry path and at impact time both low-frequency gravity waves
 420 (typically 0.01-0.001 Hz) and high-frequency acoustic waves (frequencies above 0.01 Hz,
 421 typically 1-100 Hz) (Spiga *et al.*, 2018; Revelle 1976; Garcia *et al.*, 2017; Karakostas *et al.*,
 422 2018). Those signals could be detected by a high-sensitivity pressure sensor operating
 423 continuously such as the pressure sensor in the Auxiliary Payload Sensor Suite (APSS) on board
 424 InSight (Daubar *et al.*, 2018).

425

426 An airburst signal would be characterized by two arrivals: first, the main seismic signal
 427 of surface waves excited at the location of the impact; and second, the blast wave through the
 428 atmosphere exciting the ground at the lander (Stevanović *et al.*, 2017). A differential travel time

429 of ~2 minutes is expected between two such signals due to the difference in wave propagation
430 speeds of 230 m/s in the air and 1.5 km/s in the subsurface over the 37 km distance from the
431 impact to the lander. Such a signal would be much smaller than InSight's pressure sensor limit of
432 detectability, so SEIS would be the only way to detect such a phenomenon.

433
434 Atmospheric entry modeling demonstrates that for this scale of impact the majority of the
435 meteoroid's kinetic energy is transferred to the atmosphere during deceleration and ablation, and
436 only a small fraction is directly coupled to the ground by the surviving fragment(s). The
437 relatively large blast zone surrounding the crater (Fig. 1D) is testament to this partitioning.
438 However, previous work suggests that detection of the direct ground impact is more likely than
439 detection of airburst-generated acoustic and gravity waves near the ground surface (Garcia *et al.*,
440 2017) as InSight's detection capability of acoustic and gravity waves produced by airbursts and
441 surface explosions is negatively affected by atmospheric attenuation and propagation conditions
442 less favorable than on Earth (Lognonné *et al.*, 2016). Moreover, numerical modeling (based on
443 the methodology of Karakostas *et al.*, 2018) suggests that even in the endmember case of all the
444 meteoroid kinetic energy being deposited in the atmosphere, the resulting air-coupled seismic
445 waves would still not be detectable by the InSight instruments. Acoustic ray propagation models
446 (Garcia *et al.*, 2017; Spiga *et al.*, 2018) show the trajectories of infrasound rays do not reach the
447 InSight lander, which is in an unfortunate shadow zone at this distance from the impact (Fig.
448 S11). Considering both atmospheric wave propagation conditions and meteor energy scaling, we
449 therefore do not expect the acoustic and gravity waves generated by the meteoroid that formed
450 the 1.5 m crater to be detected by InSight.

451
452

453 **3 Candidate seismic events in the time period of interest**

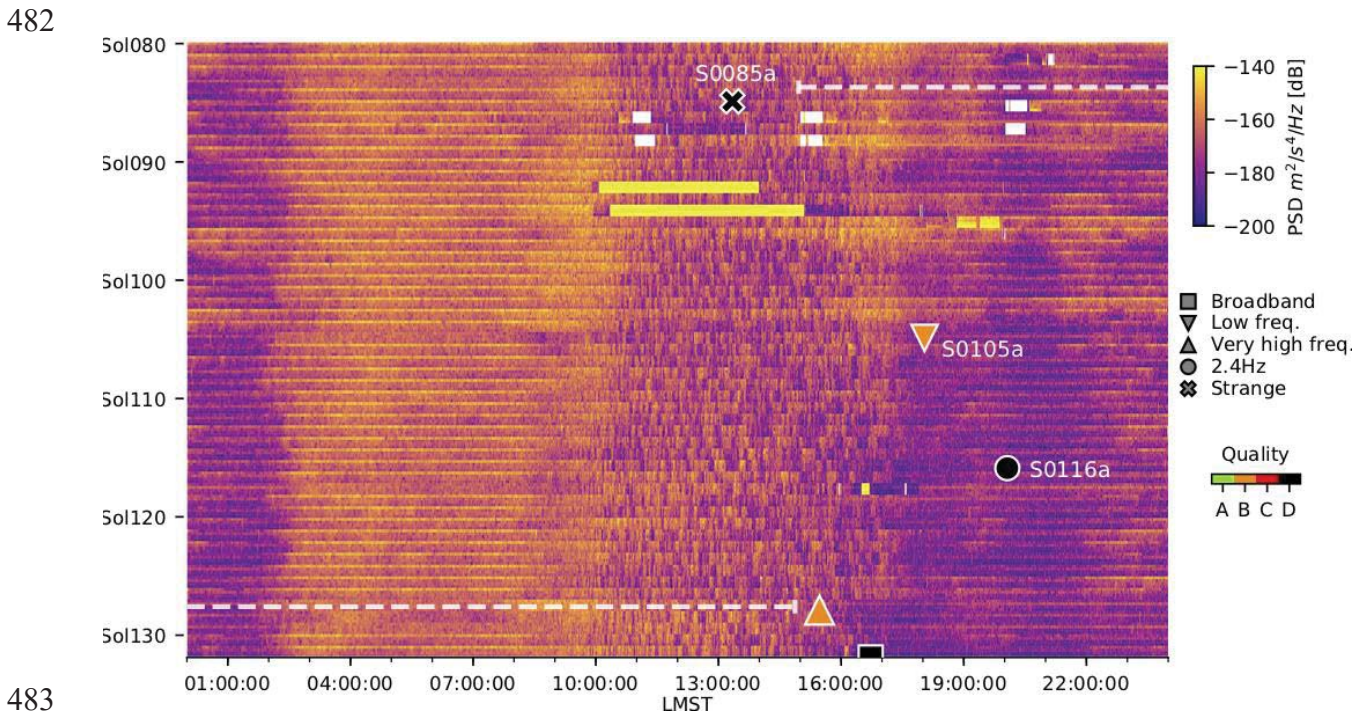
454 3.1 Description of SEIS data and the candidate events

455
456 The time between the before and after CTX images was a period of immense interest in
457 the data coming from InSight. The most relevant data was from the seismometer, Seismic
458 Experiment for Interior Structure (SEIS; Lognonné *et al.*, 2019). This temporal search window
459 occurred as SEIS commissioning was being finalized, only a few weeks after SEIS was placed
460 on the ground (17 January 2019) and the Wind and Thermal Shield (WTS) had been placed over
461 it (2 February 2019), allowing the lowest possible noise on the instrument. Fortunately,
462 continuous data collection (InSight Mars SEIS data service, 2020) had already transitioned to
463 being round-the-clock, and three-component Very-Broad-Band (VBB) and Short-Period (SP)
464 data at 10 sps, sometimes also at 20 sps, was available throughout the time period (Fig. S10).

465
466 Figure 4 provides an overview of the completeness, the noise, and the occurrence of
467 seismic signals in the data within the search window. Seismic noise on Mars clearly falls into a
468 daily pattern, with low noise only occurring between ~16:00 LMST (Local Mean Solar Time) to
469 ~02:00 LMST (Lognonné *et al.*, 2020, Giardini *et al.*, 2020). Outside of this time, there is a
470 substantial increase in noise, with steady winds in the early morning followed by a gusty midday
471 period. During these times, only very strong seismic signals can be detected. Furthermore, not all
472 days include a significant quiet period. Thus, there are large daily and day-to-day variations in

473 our capacity to detect weak seismic events on Mars using SEIS data. During the search window,
474 we estimate weak signals could be reliably detected only ~30% of the time.
475

476 Despite these limitations to the data, three potential seismic events were identified
477 between the times of the constraining CTX images (Fig. 4). Although all three are weak signals,
478 there are unique aspects of these events that deserve examination. We discuss the characteristics
479 of each of them, and the likelihood that each is the signal resulting from the observed new crater.
480
481
482



483
484 Figure 4.
485 Spectrogram stack from InSight sol 80 (16 February 2019) to sol 132 (10 April 2019). This
486 period bounds the impact search window from sol 84 14:55 LMST (21 February 2019 03:56
487 UTC) to sol 127 14:18 LMST (6 April 2019 08:20 UTC), indicated by start/end of the white
488 dashed lines. Each horizontal line in this plot corresponds to a sol-long acceleration
489 spectrogram from 20 s to 4 Hz for the vertical VBB component. White and yellow bars indicate
490 data gaps and amplitude saturation, respectively, occurring during sensor calibration and
491 hammering of the heat flow probe. The three events detected and discussed in this paper are
492 marked with symbols corresponding to the event type, while event quality is indicated by symbol
493 color (see legend). Two events that occurred just after the end of the search window are also
494 indicated.
495

496 The Marsquake Service (MQS, Clinton *et al.*, 2018) is tasked with reviewing all data
497 from SEIS, detecting and characterizing seismic energy, and maintaining a catalogue of
498 marsquakes. MQS detects events by careful manual review of all continuous data. Over the
499 course of the mission so far, the most effective approach to identifying marsquakes has proven to
500 be data review using spectrograms. Standard MQS operations produce daily spectrograms with a

501 window length of 50 seconds for frequencies below one Hz and 10 seconds for higher
502 frequencies. In the first months, two major event families have been observed (Giardini *et al.*,
503 2020; InSight Marsquake Service, 2020). The first family is characterized by events with energy
504 dominant at lower frequencies, visible as a 10-20 minute-long energy surplus between 0.1 and 3
505 Hz. This family comprises the two event types, Low Frequency (LF) and Broadband. The largest
506 of these events (named S0173a and S0235b; Giardini *et al.*, 2020, Lognonné *et al.*, 2020) have
507 clearly identifiable P- and S-waves, with clear polarization showing the direction as seen from
508 the lander, followed by long codas of scattered energy. Smaller events of this type have polarities
509 that are less clear or are not detectable, but the envelope of the waveforms and their spectral
510 content supports the interpretation that they are smaller versions of the same type of event. The
511 second major family includes High Frequency (HF) events, characterized by an energy content
512 mainly above 1 Hz, an extended coda, and a lack of polarization. An additional curious feature of
513 the InSight landing site is a local seismic resonance at 2.4 Hz. For larger HF events, the spectrum
514 can be matched by a general earthquake spectrum, taking into account source size and
515 attenuation, modulated by an amplification of 12 dB in spectral energy around 2.4 Hz. For
516 smaller HF events, only this peak is visible, while the bulk of the energy is below the ambient
517 noise level. Events in this family are classified as High Frequency, Very High Frequency, or 2.4
518 Hz. A handful of events have been documented as “Strange” if they do not fit into any of these
519 standard event types.

520

521 During the time period of the impact search, one event was found during standard MQS
522 operations. It has the label S0105a (the first seismic event to occur on sol 105 of the mission) and
523 is a Low Frequency event. It was in fact the first seismic event detected during the whole
524 mission. After the CTX discovery of the impact, a review of all data during this period was
525 performed by the InSight team, both within and independently of the MQS team. This review
526 took into account the improved understanding of marsquake character that had accumulated from
527 other events in the meantime. During this review, two additional events in the time period were
528 identified: a small High Frequency event on sol 116 and one unclassifiable seismic signal on sol
529 85. We first describe the three events in detail:

530

531 S0085a [2019/02/22 02:58:15 UTC, 13:35 LMST; MQS classification: Strange signal]

532

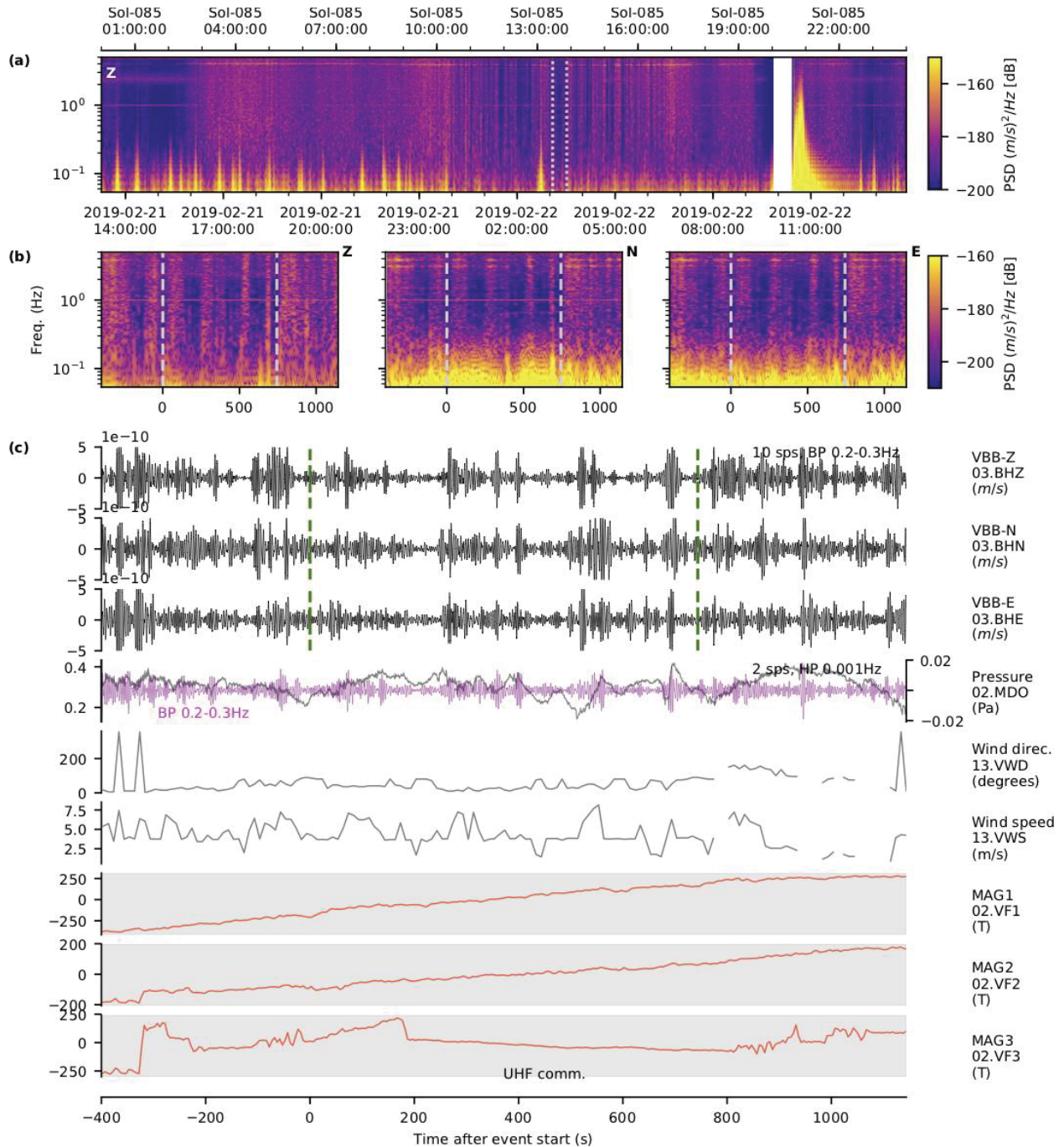
533 A summary of the S0085a event is shown in Figure 5. This event, which appears to be
534 unique among events detected on InSight thus far, consists of a very narrow-banded energy
535 surplus at 0.7 Hz, with a bandwidth of 0.05 Hz. There is a slight rise in frequency over the course
536 of the event, from 0.57 Hz up to 0.7 Hz. The signal is visible dominantly on the north
537 component, with weak traces in the Z (vertical) component. This indicates a clear N/S azimuth.
538 The signal occurs only hours after the opening of the search window, during the part of the day
539 with high atmospheric noise. In fact, it is interrupted by several wind bursts creating noise more
540 than 10 dB above the signal itself. Because it can only be resolved during the intermittent quiet
541 periods, the exact start and end times cannot be positively identified, but the event lasts at least
542 10 minutes. The very narrow bandwidth does not fit any expected seismic mechanism (including
543 impacts). A similar signal has not been observed a second time during the mission, especially not
544 during a quieter period, which would allow a better classification of its character. No particular
545 lander activity was going on at the time of this event that could explain it. Given the high

546 atmospheric noise surrounding this time, it cannot be discounted that it could be of random
547 origin.

548

549 This event was not detected using standard analysis, but extending a method that exploits
550 the ratios of the average energy residing between 2.4 Hz +/- 0.2 Hz, to different frequency bands
551 of the SP's and VBB's North, East and Vertical (Z) components. The algorithm was
552 implemented in steps of 0.4 Hz with 50% overlapping windows in frequency and avoiding
553 injection of tick noise (cross-talk noise generated by the SEIS temperature signal on the VBB
554 and SP seismic data). The resulting outliers were inspected against the average energy in the
555 Energy Short-Term Average (ESTA) channel (defined as the root mean square of data filtered
556 within a 0.5 second time window [Lognonné *et al.*, 2019]), to ensure they occurred during
557 calmer atmospheric periods, and to allow for further investigation.

558



559

560 Figure 5.

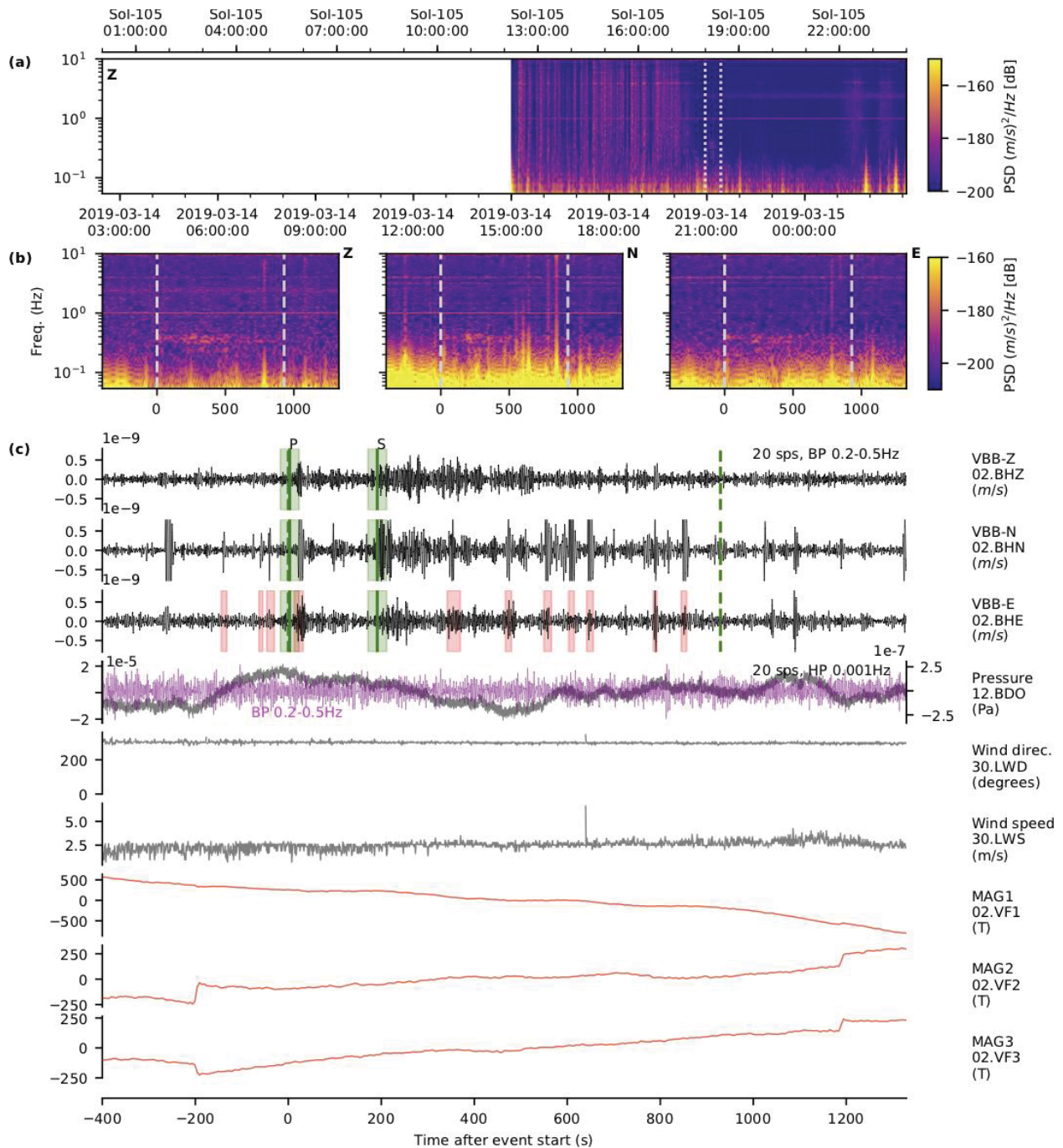
561 Summary of S0085a event. (a) provides the context of the event in the full sol spectrogram on the
 562 VBB vertical (Z) component. (b) shows spectrograms for all 3 VBB components rotated into Z,
 563 north (N) and east (E) orientations. The start and end time are indicted by the vertical dashed
 564 white lines in (a) and (b). (c) shows timeseries from the 3 VBB velocity, pressure, wind direction,
 565 wind speed, and 3 magnetometer channels. The data are filtered as indicated to accentuate
 566 seismic and pressure signals. The vertical green dotted lines in (c) indicate the event start and
 567 end times. In general in these summary figures, additional phase picks in green and glitch

568 windows in red are overlain on the seismic channels; and on the magnetometer channels
569 indications of any reported lander activity are shown in gray. For this event, however, the lander
570 has UHF communications, there are no major glitches, and the event is too weak for MQS to
571 identify phases. This event is extremely faint and not visible in the time series. The event is the
572 very narrow band of energy at 0.7 Hz visible on the N component spectrogram. As explained in
573 the text, this signal may not have a seismic source.
574

575 S0105a [2019/03/14 21:03:31, 18:07 LMST; MQS classification: Low Frequency, Quality C]

576
577 This Low Frequency event consists of two energy pulses, each without clear polarization
578 (Fig. 6). It occurs around sunset, just after the transition from the high atmospheric situation of
579 the day into the very quiet early evening. The amplitude of this event is so low that it could only
580 have been reliably detected during ~25% of the time period of the impact. The total length of the
581 signal is ~15 minutes, with at least 5 minutes uncertainty, given the relatively high noise level.
582 The spectral energy is above the ambient noise between 0.3 and 0.5 Hz for the first pulse and
583 0.15 and 0.5 Hz for the second pulse. The spectrum of the two pulses is comparable to that of
584 event S0173a, currently the largest LF event in the MQS catalog, but 16 dB lower at 0.3 Hz. The
585 phases are emergent, and phase arrival picks for the two energy pulses cannot be made in the
586 time domain, and so are made using a spectrogram and accordingly assigned high uncertainties
587 of +/-20s. In the time domain, the separation of the two pulses is also similar to that of S0173a
588 (160 seconds for S0105a vs 155 seconds for S0173a). The similarity of the signal of this event
589 and other low frequency events is shown in Fig. 3 from Giardini *et al.*, 2020, and consistent with
590 other larger events of this type, we assign P and S phases to the onset of these pulses. It would be
591 difficult to convincingly assign these phase arrivals to P and S waves without the context of the
592 wider seismicity so far recorded by InSight. Other interpretations may also be plausible, as
593 discussed above in section 2.3, though this weak event is generally similar to stronger and more
594 well-understood events.
595

596 Based on the time elapsed between these pulses, this event is estimated to be located at a
597 distance of $27 \pm 5^\circ$ (1600 ± 300 km). For S0173a, a polarization analysis was also possible,
598 resulting in a direction of the events as seen from the lander of $91 \pm 5^\circ$; thus it has been concluded
599 this is the signal of a marsquake located in the Cerberus Fossae graben system (Giardini *et al.*,
600 2020). This fault system is the only place on Mars where more than one marsquake has been
601 located so far, in agreement with pre-mission hypotheses of seismic activity there. A possible
602 interpretation of the S0105a event is therefore that it is a smaller tectonic marsquake in a similar
603 location to S0173a. As no polarization could be determined for S0105a, this interpretation must
604 remain preliminary. The low signal-to-noise ratio also implies that no depth could be estimated
605 for this or any other event in the impact time period.
606



607

608 Figure 6.

609 Summary of S0105a event, following Figure 5. During this event, there are multiple glitches (red
 610 shaded windows), most clearly visible in the E component, and no lander activity. MQS also
 611 identifies P and S phases (green solid vertical lines). Event energy is visible on all 3 components
 612 in both time series and spectrograms.

613

614 S0116a [2019/03/26 06:27:19 UTC, 20:11 LMST; MQS classification: High Frequency 2.4 Hz,
615 Quality D]

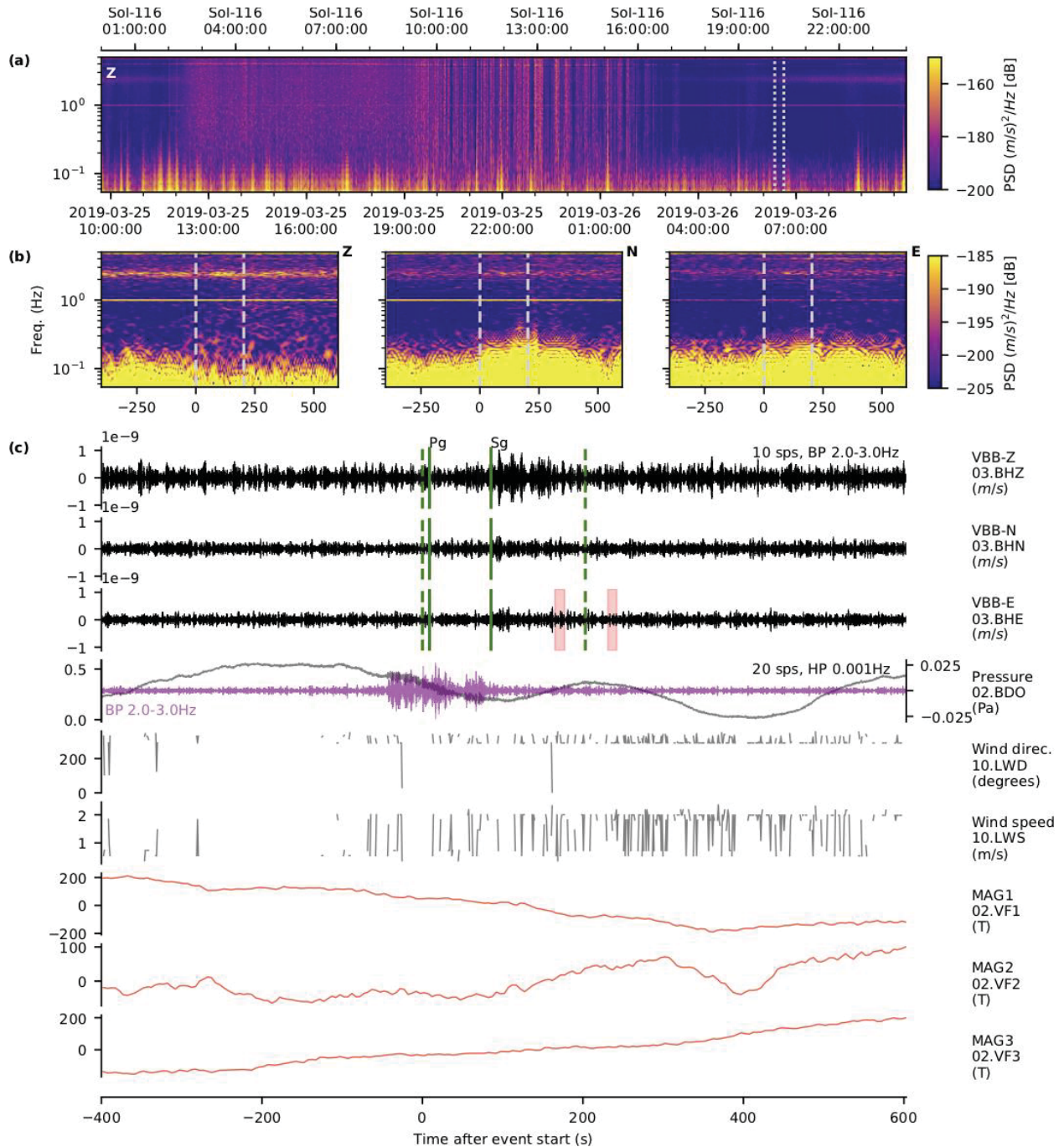
616

617 This High Frequency 2.4 Hz event, summarized in Figure 7, consists of an energy surplus
618 around the 2.4 Hz mode of about 7 dB in displacement power, concentrated into two pulses
619 separated by 78 ± 10 seconds. At the time of detection, this event was unique, but as of the time of
620 writing, we have come to realize that it was just the first occurrence of a general class of similar
621 events, termed “2.4 Hz events”. These are currently understood as being small High-Frequency
622 events. HF events are interpreted as shallow-source events occurring in a highly scattering layer
623 in the upper crust, probably shallower than the source region of the LF events. The absolute
624 distance of the HF events cannot be determined yet, as crustal seismic velocities are so far
625 unknown. The convention for these HF events is to label the start of each pulse as Pg and Sg
626 phases. From the separation of the two phases, a relative distance can be estimated. The S0116a
627 event is about four times closer than the majority of the HF events occurring later in the mission,
628 so it seems to have emanated from a different source region. Only a handful of other events
629 share a similarly short Sg-Pg interval. Nevertheless, for it to have occurred at the detected impact
630 site, the shear wave velocity in the medium would have to be as low as 210 m/s (assuming a v_p/v_s
631 ratio of $\sqrt{3}$). Such a velocity is found in bedrock layers 5-10 m deep (Lognonné *et al.*, 2020), but
632 is unlikely at these shallow depths. In the MQS catalogue, all HF events are given an estimated
633 location using an assumed S wave velocity of $v_s=2.3$ km/s, and P wave velocity of $v_p=\sqrt{3}v_s=4.0$
634 km/s. Using those assumed velocities, this event has an estimated distance of 11° , ~ 640 km from
635 the InSight lander. As the event is only visible as an excitation of the 2.4 Hz mode, its original
636 source spectrum cannot be constrained.

637

638 The amplitude of this event is so low that it could have been detected during only $\sim 20\%$
639 of the day during the time period of the known impact.

640



641

642 Figure 7.

643 Summary of S0116a event, following Figure 5. During this event, there are two minor glitches
 644 towards the end of the event (red shaded windows), and no lander activity. MQS also identifies
 645 tentative Pg and Sg phases (green vertical bars). Event energy at the 2.4 Hz resonance is weakly
 646 visible on all three components in both time series and spectrograms. An anomalous high
 647 frequency disturbance in the 2 sps pressure precedes the event, extending into the first minutes.
 648

649 We note that nearly exactly 1 sol after the search period closed, the very high frequency
650 event S0128a occurred. It can be seen in Figure 4, but outside the search period defined by the
651 dashed white lines. This was one of the largest events so far recorded, and one of the events
652 located closest to the InSight lander, although it is still estimated to be roughly $\sim 8^\circ \pm 6^\circ$ (~ 480 km
653 ± 350 km) away (Giardini *et al.*, 2020, Lognonné *et al.*, 2020). Although the uncertainties on this
654 distance estimate are large, they still do not encompass the small distance to this known impact.
655 Additionally, the timing of the CTX images has been closely compared to this event timing, and
656 the event does not fall within the possible time period for the new impact.
657
658

659 3.2 Evaluating seismic data for the candidate events

660
661 With regards to the three events detected within the search period, how can we evaluate
662 which, if any, is the recording of the known image-constrained impact? Aside from their
663 occurrence within the search period between 2/21/19 and 4/6/19, there are few other positive
664 indicators that each of the signals was caused by the impact. Scaling relationships and analog
665 comparisons predict the observed impact would create a seismic signal with peak energy \sim a few
666 Hz, with a peak amplitude of the P-wave ~ 0.8 -4 nm/s. This range is also in good agreement with
667 amplitudes from the numerical wave propagation simulations (supplemental section S2).
668 However, none of the three candidate events includes energy above 2.4 Hz. The predicted
669 duration of the event is ~ 30 seconds to one minute, although this is difficult to compare directly
670 due to scattering. However, all candidate events have durations of over several minutes. We
671 know the impact occurred at a backazimuth of 180.9° , so any polarization present in the signal
672 should be in the north-south direction. S0105a and S0116a have no indication of polarization,
673 though S0085a does include energy only in the N-S component, which is a match. Here we detail
674 how well each of the candidate signals matches these expected characteristics (Table 2).
675
676
677

678 Table 2.

679 *Expected characteristics of the seismic signal produced by the known impact, compared to the*
680 *characteristics of each of the candidate seismic events. Matching characteristics are marked*
681 *with a green check mark, non-matching characteristics are marked with a red “X”, and neutral*
682 *or undetected characteristics are marked with a black “~”. Distance to source is measured from*
683 *orbital images for the known impact and estimated for seismic events by MQS.*

	Unambiguous seismic event?	Amplitude (nm/s)	Peak Frequency (Hz)	Polarization	Duration (min)	Distance to source (km)
<i>Predicted for known impact:</i>	<i>Uncertain</i>	<i>~ 0.8-4 nm/s</i>	<i>~ 2-3 Hz most likely for body waves</i>	<i>180.9° (approximately N/S)</i>	<i>30 sec - 1 minute</i>	<i>37.4 km (0.65°)</i>
S0085a	No,	0.3 nm/s	0.7 Hz	N/S	~ 10 min	Unknown

	very unusual signal occurring in noisiest time period ~	(North; Vertical and East not above noise) (bandpass 0.5-1 Hz, 6 pole) (approximately right) ✓	(too low) ✗	✓	Too long ✗	~
S0105a	Yes, clear LF event ~	1.5 nm/s (East), 0.5 nm/s (Vertical; North affected by glitches) (bandpass 0.2-0.67 Hz, 6 pole) (approximately right) ✓	0.15-0.5 Hz (too low) ✗	None identifiable ~	~15 min Too long ✗	1600±300 km (27±5°) ✗
S0116a	No, weak 2.4 Hz resonance ~	0.7 nm/s (Vertical) 0.5 nm/s (East) 0.5 nm/s (North) (bandpass 2.2-2.8 Hz, 6 pole) (approximately right) ✓	2.4 Hz (reasonable) ✓	None identifiable ~	~3 mins Too long ✗	Unknown ~

684

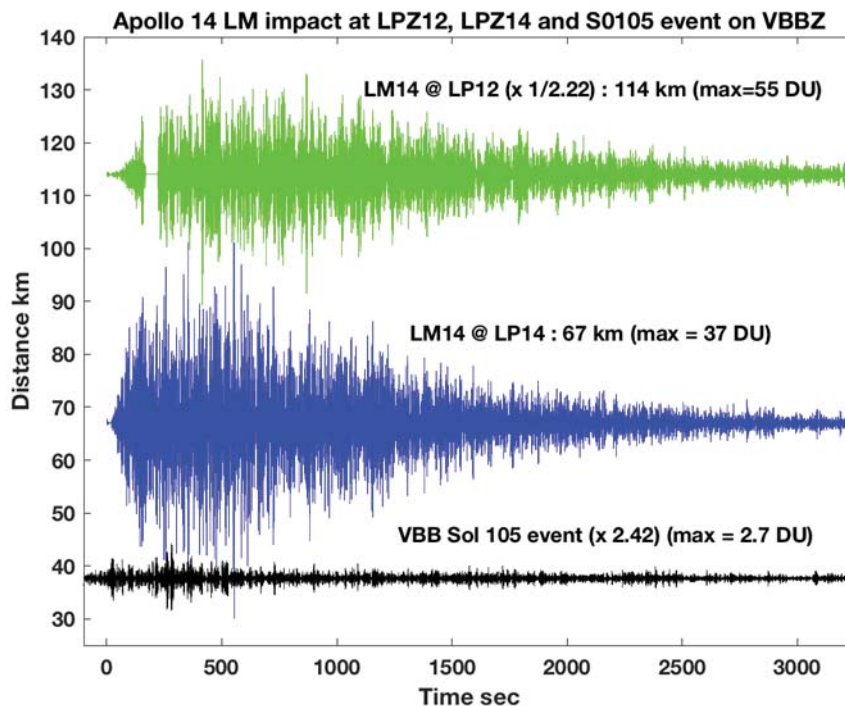
685 S0085a:

686 The event on sol 85 is the only one of the candidates with a measurable polarization, and
687 it is in the correct direction relative to the impact. However, it is possible that this event may not
688 be a seismic event at all – it could in fact be instrument-generated rather than a natural external
689 source. Many spacecraft-induced signals will have a similar N/S polarization, as the InSight
690 lander is towards the north of SEIS. Compared to other observed events, it has very narrow-band
691 energy with an apparent dispersion, which is not expected for an impact. Even if this were a true
692 seismic event, we cannot definitively identify it with the impact.
693

694 S0105a:

695 The event on sol 105, on the other hand, is a clear seismic event. Its amplitude (0.5 nm/s
696 in the 0.2-0.67 Hz bandwidth on Vertical and 1.5 nm/s on East) is at the lower end of that
697 predicted. The spectral peak is at a frequency lower than that predicted. If this is an impact at
698 ~40 km, it would have to be explained why tens of other seismic events detected so far look very
699 similar to this one. It is exceedingly unlikely that multiple small impacts occurred in this region
700 in the same time period and we do not have any images of them; although we do not have
701 complete repeat image coverage of the region out to ~40 km away from InSight in order to rule
702 this out completely. Without definitive criteria for discriminating between impact and tectonic
703 sources (see Section 4.1), we cannot exclude the possibility that one of these similar events is
704 also an impact.
705

706 Figure 8 compares the S0105a signal with two Apollo impact records. All signals have
707 been filtered with a 6th-order Butterworth bandpass (0.2-0.67 Hz), and SEIS data are expressed in
708 Apollo Digital Units (DU). Amplitudes in Fig. 8 have been corrected with respect to distance
709 using a -1.5 power law dependency with respect to the Apollo 14 LM impact recorded by the
710 Apollo 14 LP seismometer, while the non-corrected amplitudes are given for each trace. The
711 amplitude of the S0105 event is approximately 15 times smaller than that of the lunar LM
712 impacts, which is within our estimate of a factor of 3.5-210 (see Section 2.3). The amplitude of
713 the signal at 0.5 Hz can therefore be explained by the size of the known impact. However,
714 neither the lack of high frequencies nor the duration of this event are compatible with what we
715 expect for this impact.
716
717



718

719 Figure 8.

720 *Comparison between the martian event S0105a (black) and the Apollo 14 LM impact as*
721 *recorded at two Apollo stations (green for Apollo 12 and blue for Apollo 14). The S0105a event*
722 *has been deglitched (Lognonné et al., 2020) and converted into Apollo data units (DU) by using*
723 *the Apollo Transfer function of the LP instruments. All events have been filtered with a 6th order*
724 *Butterworth bandpass between 0.2 and 0.67 Hz and corrected for the different distances by*
725 *using a -1.5 power law with distance. Amplitude in DU as well as geometrical correction values*
726 *are given on the figure. The very impulsive first arrival identified by MQS for S0105a is at time*
727 *0, followed by a second arrival 160 seconds later.*
728

729 S0116a:

730 The event on sol 116 has an amplitude at the lower end of that predicted, though this is
731 on top of the 2.4 Hz resonance, so is likely amplified. It has a higher frequency than the other
732 events, which is reasonable for a small, local event. No polarization was detected, so no direction
733 or distance can be estimated. In the months since this event was recognized, hundreds of other
734 similar events have occurred, again making it unlikely this is due to an impact, which would
735 occur relatively infrequently.

736
737 In summary, none of the three events can be unambiguously identified as the seismic
738 signature of the new impact. The S0105a event can be explained as a relatively small tectonic
739 marsquake in the Cerberus Fossae region. The S0116a could possibly be caused by the impact,
740 but given its low amplitude, it cannot be further classified or analyzed. Both S0105a and S0116a
741 are similar to numerous other events in the marsquake catalogue, suggesting they are not
742 produced by a local impact signal, which we expect to be a rare occurrence. The S0085a signal is
743 extremely weak, and its very narrow-band nature suggests it is not likely to have been caused by
744 an external seismic event.

745
746 We note the extreme variation in diurnal noise means that significantly larger events than
747 the three identified here may be hidden in the data. As noted, the amplitude we predict for this
748 impact is quite close to the measured noise levels of SEIS during the least noisy time periods
749 (Fig. 4). Given daily and seasonal variations in temperature and wind activity, the noise levels
750 are lowest in the evening (Lognonné et al., 2020; Fig. 4). Signals on the order of the predicted
751 amplitude would only be observable (at ~3 SNR) for ~20-30% of the time. Thus, the actual
752 signal from this impact could very likely have occurred at a time when noise swamped the
753 signal.

754
755 Another observational bias could occur due to the 2.4 Hz signals. These are a resonance
756 seen in numerous other events (Giardini et al., 2020), and this is also near the peak frequency
757 expected for impact event. Such a resonance could enhance smaller signals, allowing detection
758 of signals that are otherwise ~ten times smaller if they are near the resonance. This might help
759 our detection likelihood, but it is also a narrow band, making source discrimination more
760 difficult.

761

3.3 Evaluating atmospheric data for the candidate events

Although no obvious atmospheric signals were associated with the three seismic candidates, each event was investigated to eliminate that possibility:

S0085a occurred in the local early afternoon (unlike the S0105a and S0116a events). Atmospheric variability for S0085a is thus mostly governed by convective turbulence (cells and vortices), usually found in daytime hours. There were no vortex signals close to the event that might have affected the seismic signal. Under normal conditions, gravity waves are not usually detected in daytime hours, based on the first 300 sols of InSight measurements (Banfield *et al.*, 2020), and no gravity waves were detected around the time of this event.

There was no notable atmospheric signal associated directly with the S0105a event. Pressure and temperature measurements were uneventful, and the wind was steady and low. Two hours after the seismic event, a gravity wave of strong amplitude (± 0.5 Pa) with a period of 400-600 seconds was detected. However, between sols 100-150, similar signals were very frequently seen at these local times ($\sim 20:00$ LMST). Furthermore, given the proximity of the impact to InSight, a propagation speed that would cause a two hour delay between the seismic signal and the atmospheric wave packet is far too low to be realistic. This is based on typical gravity wave phase speeds estimated by Banfield *et al.* (2020) of ~ 20 -30 m/s. The gravity wave signal reached InSight two hours after the seismic event; even accounting for background wind, the gravity wave would be too fast to have been emitted by the atmospheric entry of a meteoroid at 37.4 km distance. It is thus not likely to be related to the seismic event.

For S0116a, a gravity wave signal was found in the pressure signal at a time near the seismic event. However, it started about a quarter of an hour before the seismic signal, which implies the two are unrelated. Wind and temperature measurements behaved as usual for evening conditions at the InSight landing site. Interestingly, around the start of the event, just before the seismic signal, the pressure signal also underwent high-frequency fluctuations in the infrasonic range (*i.e.* < 20 Hz). Though an impulsive pressure signal could be expected from a close impact event, the long duration HF pressure wave packet we observed is similar to scattered pressure signals related to explosions seen in infrasound records on Earth (Green *et al.*, 2011). Such scatterings of acoustic energy can occur when small-scale gravity waves perturb the lower atmosphere wave guide (e. g. Green *et al.*, 2011; Damiens *et al.*, 2017). Nonetheless, other facts concur to put aside the impact hypothesis as a source of the observed pressure fluctuations: (1) high-frequency pressure fluctuations are recorded by InSight almost every sol in the evening, (Banfield *et al.*, 2020), (2) acoustic propagation models (Garcia *et al.*, 2017; Spiga *et al.*, 2018) show that the InSight lander is in a shadow zone for infrasound waves generated at the impact location (Fig. S11) and (3) owing to the noise levels of the respective instruments, if infrasound signals were seen in InSight pressure data, they would also be seen in the seismic data. They would also have to be at a significantly larger distance than this case (Martire *et al.*, 2020). This makes it very difficult to ascribe these particular pressure fluctuations to the sol 116 seismic event, or to any impact-induced phenomena at the distance of the known impact.

Regarding an airburst signal, none of the candidate events have two distinct arrivals with the expected temporal spacing of ~ 2 minutes (Section 2.4), even if they were above the detection

808 threshold. So we do not believe an impact airburst was detected for this event. To summarize,
809 while interesting atmospheric signals were noticed during the three events, they are not likely
810 related to either the seismic events in question or to the impact event.
811

812 4 Discussion

813 4.1 Re-assessment of seismic impact discriminators

814
815 Over the first months of the InSight mission, we have learned that marsquakes (whether
816 sources are impact or tectonic) differ from our previous experience with either terrestrial or lunar
817 analogs. The impact discriminators we planned on using before arriving at Mars (Daubar *et al.*,
818 2018) have limited utility given the reality of martian seismic signals recorded thus far. The
819 marsquakes observed so far are small in amplitude, with surprisingly long durations, and with
820 apparently low attenuation / high Q. This makes many of these characteristics difficult to
821 distinguish. We re-assess (*in italics*) each of those planned discriminators in light of real seismic
822 data from InSight:
823

- 824 1) First motion: Impacts create positive pressure impulses, creating a positive first motion,
825 in a direction away from the source.
 - 826 ▪ *Despite the low noise recorded by InSight during periods of the day, marsquake*
827 *signals have proven to be very small. In all but the largest signals seen so far,*
828 *phase arrivals are emergent, so noise obscures the direction of first arrivals.*
829 *Scattering in the regolith randomizes the energy.*
 - 830 ▪ *Even if we had clear first motions, quakes with a double couple source would*
831 *have a positive first motion 50% of the time anyway, assuming a random*
832 *orientation of sources.*
- 833 2) S-wave energy: Impacts produce more P-waves than S-waves.
 - 834 ▪ *A quake could also have low S energy for an unfavorable source orientation.*
 - 835 ▪ *S-waves are obscured by scattered P energy, so this is hard to determine for small*
836 *events.*
- 837 3) Magnitude ratio: Impacts produce fewer surface waves, so impacts should have a strong
838 difference between magnitudes based on body waves and those based on surface waves.
 - 839 ▪ *Surface waves are not being detected for any martian events (Giardini et al.,*
840 *2020). The absence or diminished presence of surface wave energy, therefore,*
841 *cannot be used as an impact discriminator, because all events lack surface waves.*
- 842 4) Frequency content: Different source mechanisms lead to a smaller cutoff frequency for
843 impacts.
 - 844 ▪ *Cutoff frequencies for the largest of the detected martian events, where they can*
845 *be determined, are typically near 6 Hz but can rise up to 12 Hz (Giardini et al.,*
846 *2020). This cutoff frequency is much higher than the ~1-3 Hz expected for impacts*
847 *(Daubar et al., 2018).*
- 848 5) Depth phases: Impacts occur at the surface, implying no depth reflected phases.
 - 849 ▪ *Additional phases beyond P and S arrivals have not been identified in any events*
850 *thus far (Giardini et al., 2020) because of scattering and the resulting extended*
851 *codas, so a lack of depth phases cannot be used to indicate an impact.*

852

853 4.2 Revised predictions of impact detections by InSight

854

855 As this is the only impact known to have occurred this close to InSight during its prime
856 science monitoring phase thus far, we wish to evaluate how likely this particular impact event
857 was. Using an estimated current cratering rate, we can estimate the probability of a ~1 m
858 diameter crater forming within ~50 km of InSight in one Earth year. Unfortunately, the cratering
859 rate for impacts of this scale is not well constrained. As an estimate, we use a production
860 function based on an extrapolation of the fragmentation model of Williams *et al.* (2014) pinned
861 to the production function based on observed dated craters from Daubar *et al.* (2013) (see
862 Teanby 2015 for more details). The resulting rate is $\sim 2 \times 10^{-5}$ impacts >1 m diameter/km²/Earth
863 year. The uncertainty on this value is probably at least a factor of 10 in both directions. For this
864 impact rate, the probability of one impact in any given circle of radius 50 km each Earth year is
865 ~ 0.2 . Thus this event is not completely unlikely, but we were quite lucky to catch it in the
866 images, which have covered only a small fraction of that area multiple times since InSight
867 landed.

868

869 Based on measured noise levels of SEIS on the ground at Mars, we can revise our pre-
870 landing estimates of the number and size of impact detections to expect during the InSight
871 mission. Teanby and Wookey (2011) and Teanby (2015) estimated seismic impact detection
872 rates with predicted Mars seismic noise. We can now update these predictions using measured
873 noise levels from the first few months of InSight operations. Teanby and Wookey (2011) model
874 results for large impacts predict their peak seismic energy will be in the 1-2 Hz frequency range
875 (where the SEIS-VBB instrument is most sensitive). Teanby (2015) compiled observations from
876 small impacts and explosions to suggest that their peak seismic energy will be in the 1-8 Hz
877 frequency range (where the SEIS-SP instrument is most sensitive). Typical SEIS noise levels are
878 $0.3-10 \times 10^{-9}$ m/s²/Hz^{1/2} in the 1-8 Hz range (Lognonné *et al.*, 2020), although during much of the
879 martian day SEIS sees considerably higher noise than these levels. Using scaling relationships
880 developed in previous work (Teanby, 2015; Teanby and Wookey 2011), we can predict P-wave
881 amplitudes for different size impacts at various distances (Fig. 2). To get the expected frequency
882 of impacts of different sizes, we use the production function developed by Teanby (2015) that
883 uses new dated craters from Daubar *et al.* (2013) extrapolated to smaller diameters to account for
884 the observational rollover using the Williams *et al.* (2014) fragmentation model. As signals at the
885 noise level are very difficult to detect (as demonstrated by this paper!), we use a more
886 conservative restriction of SNR ~ 3 to be realistic. InSight's noise measurements show that the
887 martian day can be roughly split into low-noise and high-noise time periods. Assuming a typical
888 low noise level of 1.5×10^{-9} m/s²/Hz^{1/2} at 4 Hz (Lognonné *et al.*, 2020) is appropriate
889 approximately 50% of the time, and the remaining 50% of the time it is too noisy for any
890 detections, we predict just ~ 2 detections of impact events per Earth year, during times when
891 higher continuous rate data are collected. Furthermore, seismic amplitudes of signals from small
892 craters could be even lower (Wójcicka *et al.*, 2020) resulting in even fewer detections. There are
893 still large uncertainties on the predicted detection rate, at least an order of magnitude. However,
894 given that we have yet to unambiguously detect any impacts in the seismic data, either the large
895 end of this range is increasingly unlikely, or – more likely – we have not yet learned enough
896 about martian seismic signals to recognize impacts in the data.

897
898
899
900
901
902
903
904
905
906
907

Because of this revised expectation of seismic detections of impacts, we have reversed our operational approach to detecting impacts. Instead of examining the seismic data for possible impact-induced signals, then following up with orbital images appropriate for the expected size and location of the impact, as described in Daubar *et al.* (2018), we are instead examining orbital images for new impacts, as indicated by dark spots or albedo changes near InSight. When more of these are found, we will examine the seismic data during the image-constrained time periods in a manner similar to the analysis presented here.

908 **5 Conclusions**

909
910
911
912
913
914
915
916
917
918
919
920
921
922

The exciting and lucky observation of a new impact occurring very close to the InSight lander during its prime mission presented a first opportunity to test our understanding of the seismic detectability of small impacts on Mars. Three potential candidate events were identified in the seismic data during the time period constrained by the before and after orbital CTX images; however, we are not able to determine that any of those seismic or atmospheric signals were definitively associated with that impact event. This is mainly because although the impact was nearby, it was quite small, forming only a ~ 1.5 m diameter crater, and likely was created by a significantly decelerated impactor. We predict that the signals produced by this impact were very close to the measured minimum noise amplitudes seen by the InSight seismometers, and for a good portion of the time, the observed noise levels are well above the predicted impact signal amplitude. Thus a lack of detection for an impact of this size and at this location is disappointing, but not surprising.

923
924
925
926
927
928
929
930
931
932
933
934
935
936
937

There are many uncertainties in our predictions of seismic signals from the known impact, for example in converting crater size to seismic moment. The attenuation and scattering properties of the martian crust are not yet completely understood, nor is the velocity structure of the subsurface. Given the uncertainties in our predictions, it is still possible that the known crater was indeed responsible for one of the three candidate seismic events, although we cannot support that conclusion with our current knowledge. As InSight reveals more about the properties of the martian interior, the uncertainties in our predictions will be reduced. Future efforts at numerical modeling of this specific impact and coupled seismic modeling of the resulting wave propagation may reveal additional things to look for in the seismic or atmospheric data that may allow us to identify future impacts, if not this particular event. As we did not positively detect this impact in the data, we can at least conclude that we are not grossly underestimating the seismic amplitudes from impact events. Likewise, we see no definitive signals associated with this impact in the atmospheric data, nor do we expect that would be likely in this specific case.

938
939
940
941

The process of searching within the continuous seismic data from InSight for evidence of an event associated with an image-constrained impact has refined our understanding of impact-generated seismic signals through forward modelling and allowed us to reevaluate our predictions of impact detectability. Using the now-known noise levels of the SEIS instrument on

942 Mars, we expect ~2 impact detections with SNR>3 each Earth year. This is assuming continued
943 high sampling rates able to detect higher frequency peaks, which have lately begun. Our
944 continued efforts to search orbital images for new dated impacts near InSight will almost
945 certainly result in more image-constrained impacts. This work has provided a template workflow
946 to help us quickly identify future impact seismic signals associated with image-detected craters.
947 We continue to listen for impacts on Mars.

948
949
950

951 **Acknowledgements**

952 We thank the CTX and HiRISE operations teams for the initial identification of the site, and
953 careful and timely acquisition of the images used to make this discovery. We acknowledge
954 NASA, CNES, their partner agencies and Institutions (UKSA, SSO, DLR, JPL, IPGP-CNRS,
955 ETHZ, IC, MPS-MPG) and the flight operations team at JPL, SISMOC, MSDS, IRIS-DMC and
956 PDS for acquiring and providing InSight data, including SEED SEIS data. We thank two
957 anonymous reviewers for their constructive input.

958

959 IJD is supported by NASA InSight Participating Scientist grant 80NM0018F0612. NAT, JW &
960 AH are supported by UK Space Agency grant ST/R002096/1. The French Team acknowledge
961 the French Space Agency CNES and ANR (ANR-14-CE36-0012-02, ANR-19-CE31-0008-08).
962 The Swiss co-authors were jointly funded by (1) Swiss National Science Foundation and French
963 Agence Nationale de la Recherche (SNF-ANR project 157133 “Seismology on Mars”), (2) Swiss
964 State Secretariat for Education, Research and Innovation (SEFRI project “MarsQuake Service-
965 Preparatory Phase”) and (3) ETH Research grant ETH-06 17-02. GSC & NW are supported by
966 STFC grants ST/S000615/1, ST/S001514/1. KM and AR are fully supported by the Australian
967 Research Council (DP180100661 and DE180100584). A part of the 3-D simulations in the
968 supplementary material was performed on the Earth Simulator of the Japan Agency for Marine-
969 Earth Science and Technology (JAMSTEC), another part on resources provided by the Los
970 Alamos National Laboratory Computing Program supported by DOE. A portion of this research
971 was carried out at the Jet Propulsion Laboratory, California Institute of Technology, under a
972 contract with the National Aeronautics and Space Administration. This is InSight contribution
973 number 104 and IPGP contribution XXX.

974

975 All data used in this work are publicly available via the Planetary Data System (PDS;
976 <https://pds.nasa.gov/>). Specifically, CTX images can be found at [https://pds-
977 imaging.jpl.nasa.gov/volumes/mro.html](https://pds-imaging.jpl.nasa.gov/volumes/mro.html), HiRISE images can be found at
978 <https://www.uahirise.org/>, and InSight APSS/TWINS/PS data can be found at
979 https://atmos.nmsu.edu/data_and_services/atmospheres_data/INSIGHT/insight.html. InSight
980 SEIS data is available in the form of a seismic event catalogue (DOI: 10.12686/a6) and
981 waveform data (DOI: 10.18715/SEIS.INSIGHT.XB_2016) that are publicly available from the
982 IPGP Datacenter and IRIS-DMC, as well as raw data available in the PDS at [https://pds-
983 geosciences.wustl.edu/missions/insight/seis.htm](https://pds-geosciences.wustl.edu/missions/insight/seis.htm). Apollo seismic data are available in raw form at
984 <https://darts.isas.jaxa.jp/planet/seismology/apollo/index.html>, and the data are available in SEED
985 format from the IPGP Data Center for lunar data (Code XA, <http://datacenter.ipgp.fr/data.php>).

986 Seismic modeling results and parameters are available on the IPGP data center at
987 https://doi.10.18715/JGR_NewCraterMod_2020.
988
989

990 **References**

- 991 Banfield, D. *et al.* (2020) First results from InSight’s meteorology station on Mars. *Nature*
992 *Geoscience*, 13, pp. 190-198. DOI: 10.1038/s41561-020-0534-0
- 993 Clinton, J., Giardini, D., Böse, M., S. Ceylan, M. van Driel, F. Euchner, R. F. Garcia, S.
994 Kedar, A. Khan, S. C. Stähler, B. Banerdt, P. Lognonné, E. Beucler, I. Daubar, M.
995 Drilleau, M. Golombek, T. Kawamura, M. Knapmeyer, B. Knapmeyer-Endrun, D.
996 Mimoun, A. Mocquet, M. Panning, C. Perrin, N. A. Teanby, The Marsquake Service:
997 Securing Daily Analysis of SEIS Data and Building the Martian Seismicity Catalogue
998 for InSight, *Space Sci Rev* (2018) 214: 133. [https://doi.org/10.1007/s11214-018-0567-](https://doi.org/10.1007/s11214-018-0567-5)
999 5
- 1000 Damians, F., C. Millet, and F. Lott, 2017: An investigation of infrasound propagation over
1001 mountain ranges, *Journal of the Acoustical Society of America*, 2018, 143:1, 563-574
- 1002 Daubar, I. J., McEwen, A. S., Byrne, S., Kennedy, M. R., Ivanov, B., 2013. The current martian
1003 cratering rate. *Icarus* 225, 506–516.
- 1004 Daubar, I., Lognonné, P., Teanby, N.A., Miljkovic, K., Stevanović, J., Vaubaillon, J., Kenda, B.,
1005 Kawamura, T., Clinton, J., Lucas, A., Drilleau, M., Yana, C., Collins, G.S., Banfield, D.,
1006 Golombek, M., Kedar, S., Schmerr, N., Garcia, R., Rodriguez, S., Gudkova, T., May, S.,
1007 Banks, M., Maki, J., Sansom, E., Karakostas, F., Panning, M., Fuji, N., Wookey, J., van
1008 Driel, M., Lemmon, M., Ansan, V., Böse, M., Stähler, S., Kanamori, H., Richardson, J.,
1009 Smrekar, S., Banerdt, W.B., 2018. Impact-Seismic Investigations of the InSight Mission.
1010 *Space Sci Rev* 214, 132. <https://doi.org/10.1007/s11214-018-0562-x>
- 1011 Daubar, Ingrid Justine, M. E. Banks, N. C. Schmerr, and Matthew P. Golombek. 2019. “Recently
1012 Formed Crater Clusters on Mars.” *Journal of Geophysical Research: Planets*.
1013 <https://doi.org/10.1029/2018JE005857>.
- 1014 Garcia, Raphaël F., Quentin Brissaud, Lucie Rolland, Roland Martin, Dimitri Komatitsch,
1015 Aymeric Spiga, Philippe Lognonné, and William Bruce Banerdt. 2017. “Finite-
1016 Difference Modeling of Acoustic and Gravity Wave Propagation in Mars Atmosphere:
1017 Application to Infrasonds Emitted by Meteor Impacts.” *Space Science Reviews* 211 (1–
1018 4): 547–70. <https://doi.org/10.1007/s11214-016-0324-6>.
- 1019 Giardini, D., Lognonné, P., Banerdt, W.B. et al. The seismicity of Mars. *Nat. Geosci.* 13, 205–
1020 212 (2020). <https://doi.org/10.1038/s41561-020-0539-8>
- 1021 Gillet, K., L. Margerin, M. Calvet, and M. Monnereau (2017) Scattering attenuation profile of
1022 the Moon: Implications for shallow moonquakes and the structure of the megaregolith.
1023 *Physics of the Earth and Planetary Interiors* 262, 28-40. DOI:10.1016/j.pepi.2016.11.001
- 1024 Golombek, M. P. *et al.* (2020) “Geology of the InSight Landing Site on Mars.” *Nature*
1025 *Communications*, 11, 1014. <https://doi.org/10.1038/s41467-020-14679-1>.

- 1026 Green, D. N., Julien Vergoz, Robert Gibson, Alexis Le Pichon, Lars Ceranna. (2011) Infrasound
 1027 radiated by the Gerdec and Chelophechene explosions: propagation along unexpected
 1028 paths, *Geophysical Journal International*, Volume 185, Issue 2, Pages 890–910,
 1029 <https://doi.org/10.1111/j.1365-246X.2011.04975.x>
- 1030 Gudkova, T., Lognonné, P. , Gagnepain-Beyneix, J., 2011. Seismic source inversion for Large
 1031 impacts detected by the Apollo seismometers, *Icarus*, **211**, 1049-1065, doi :
 1032 [10.1016/j.icarus.2010.10.028](https://doi.org/10.1016/j.icarus.2010.10.028).
- 1033 Gudkova, Tamara V., Philippe Lognonné, Katarina Miljković, and Jeannine Gagnepain-Beyneix.
 1034 2015. “Impact Cutoff Frequency – Momentum Scaling Law Inverted from Apollo
 1035 Seismic Data.” *Earth and Planetary Science Letters* 427: 57–65.
 1036 <https://doi.org/10.1016/j.epsl.2015.06.037>.
- 1037 Holsapple, K.A., 1993. The scaling of impact processes in planetary sciences. *Ann. Rev. Earth*
 1038 *Planet. Sci.* 21, 333–373. <https://doi.org/10.1146/annurev.ea.21.050193.002001>
- 1039 Holsapple, K.A., Housen, K.R., 2007. A crater and its ejecta: An interpretation of Deep Impact.
 1040 *Icarus* 187, 345--356. <https://doi.org/10.1016/j.icarus.2006.08.029>
- 1041 InSight Mars SEIS data Service (2019) SEIS raw data, InSight Mission. IPGP, JPL, CNES,
 1042 ETHZ, ICL, MPS, ISAE-Supaero, LPG, MSFC. Other/Seismic Network,
 1043 https://doi.org/10.18715/SEIS.INSIGHT.XB_2016
- 1044 InSight Marsquake Service (2020) Mars Seismic Catalogue, InSight Mission; V1 2/1/2020.
 1045 ETHZ, IPGP, JPL, ICL, ISAE-Supaero, MPS, Univ Bristol. Dataset.
 1046 <http://doi.org/10.12686/a6>
- 1047 JeongAhn, Youngmin, and Renu Malhotra. 2015. “The Current Impact Flux on Mars and Its
 1048 Seasonal Variation.” *Icarus* 262: 140–53. <https://doi.org/10.1016/j.icarus.2015.08.032>.
- 1049 Karakostas, Foivos, Virgile Rakoto, Philippe Lognonné, Carene Larmat, Ingrid Justine Daubar,
 1050 and Katarina Miljković. 2018. “Inversion of Meteor Rayleigh Waves on Earth and
 1051 Modeling of Air Coupled Rayleigh Waves on Mars.” *Space Science Reviews* 214 (8):
 1052 127. <https://doi.org/10.1007/s11214-018-0566-6>.
- 1053 Komatitsch, D. and Tromp, J., 2002. Spectral-element simulations of global seismic wave
 1054 propagation—I. Validation. *Geophysical Journal International*, 149(2), pp.390-412.
- 1055 Leng, K., Nissen-Meyer, T. and van Driel, M., 2016. Efficient global wave propagation adapted
 1056 to 3-D structural complexity: a pseudospectral/spectral-element approach. *Geophysical*
 1057 *Supplements to the Monthly Notices of the Royal Astronomical Society*, 207(3),
 1058 pp.1700-1721.
- 1059 Le Feuvre, M, and Mark A. Wieczorek. 2008. “Nonuniform Cratering of the Terrestrial Planets.”
 1060 *Icarus* 197 (1): 291–306. <https://doi.org/10.1016/j.icarus.2008.04.011>.

- 1061 Lesage, P., M. J. Heap, and A. Kushnir (2018) A generic model for the shallow velocity structure
1062 of volcanoes. *Journal of Volcanology and Geothermal Research* 356, 114-126.
1063 DOI:10.1016/j.jvolgeores.2018.03.003
- 1064 Lognonné, P., Banerdt, W.B., Pike, W.T. et al. Constraints on the shallow elastic and anelastic
1065 structure of Mars from InSight seismic data. *Nat. Geosci.* 13, 213–220 (2020).
1066 <https://doi.org/10.1038/s41561-020-0536-y>
- 1067 Lognonné, P., Banerdt, W.B., Giardini, D. *et al.*, SEIS: Insight’s Seismic Experiment for
1068 Internal Structure of Mars, *Space Sci Rev* (2019) 215: 12.
1069 <https://doi.org/10.1007/s11214-018-0574-6>
- 1070 Lognonné, P., Karakostas, F., Rolland, L. and Nishikawa, Y., 2016. Modeling of atmospheric-
1071 coupled Rayleigh waves on planets with atmosphere: From Earth observation to Mars
1072 and Venus perspectives. *The Journal of the Acoustical Society of America*, 140(2),
1073 pp.1447-1468.
- 1074 Lognonné, P., M. Le Feuvre, C. L. Johnson, and R. C. Weber (2009), Moon meteoritic seismic
1075 hum: steady state prediction, *J. Geophys. Res.*, **114**, E12003, doi:10.1029/2008JE003294.
- 1076 Maeda, T., Takemura, S. and Furumura, T., 2017. OpenSWPC: an open-source integrated
1077 parallel simulation code for modeling seismic wave propagation in 3D heterogeneous
1078 viscoelastic media. *Earth, Planets and Space*, 69(1), p.102.
- 1079 Malin, Michael C., James F. Bell, Bruce A. Cantor, Michael a. Caplinger, Wendy M. Calvin, R.
1080 Todd Clancy, Kenneth S. Edgett, *et al.*, 2007. “Context Camera Investigation on Board
1081 the Mars Reconnaissance Orbiter.” *Journal of Geophysical Research* 112 (E5): E05S04.
1082 <https://doi.org/10.1029/2006JE002808>.
- 1083 Martire L., R. Garcia, L. Rolland, A. Spiga, P. Lognonné, D. Banfield,
1084 W. B. Banerdt, R. Martin (2020) Martian Infrasound: Numerical Modeling and Analysis
1085 of InSight's Data. *Journal of Geophysical Research (Planets)*, submitted.
- 1086 McEwen, Alfred S., Eric M. Eliason, James W. Bergstrom, Nathan T. Bridges, Candice J.
1087 Hansen, W. Alan Delamere, John a. Grant, *et al.*, 2007. “Mars Reconnaissance Orbiter’s
1088 High Resolution Imaging Science Experiment (HiRISE).” *Journal of Geophysical
1089 Research* 112 (E5): E05S02. <https://doi.org/10.1029/2005JE002605>.
- 1090 McMullan, S. and G. S. Collins (2019) Uncertainty quantification in continuous fragmentation
1091 airburst models. *Icarus* 327, 19-35. DOI:10.1016/j.icarus.2019.02.013
- 1092 Moore, H. J. (1976) Missile impact craters (WSPR, New Mexico) and applications to lunar
1093 research, Geological Survey Professional Paper 812-B, (contributions to Astrogeology).
- 1094 Nissen-Meyer, T., Driel, M.V., Stähler, S., Hosseini, K., Hempel, S., Auer, L., Colombi, A. and
1095 Fournier, A., 2014. AxiSEM: broadband 3-D seismic wavefields in axisymmetric media.
1096 *Solid Earth*, (1), pp.425-445.

- 1097 Parker, Timothy J., Matthew P. Golombek, F. J. Calef, N. R. Williams, S. LeMaistre, W.
 1098 Folkner, Ingrid Justine Daubar, *et al.*, 2019. “Localization of the InSight Lander.” *50th*
 1099 *Lunar and Planetary Science Conference, Held 18-22 March, 2019 at The Woodlands,*
 1100 *Texas. LPI Contribution No. 2132, Id.1948 50.*
 1101 <http://adsabs.harvard.edu/abs/2019LPI....50.1948P>.
- 1102 Plescia, J.B., Robinson, M.S., Wagner, R., Baldrige, R., 2016. Ranger and Apollo S-IVB
 1103 spacecraft impact craters. *Planetary and Space Science* 124, 15–35.
 1104 <https://doi.org/10.1016/j.pss.2016.01.002>
- 1105 Revelle, D.O., P.G. Brown, P. Spurny, Entry dynamics and acoustics/infrasonic/seismic analysis
 1106 for the ` Neuschwanstein meteorite fall. *Meteorit. Planet. Sci.* 39(10), 1605–1626 (2004)
- 1107 Rivoldini, A., Van Hoolst, T., Verhoeven, O., Mocquet, A. and Dehant, V., 2011. Geodesy
 1108 constraints on the interior structure and composition of Mars. *Icarus*, 213(2), pp.451-472.
- 1109 Sato, H. and M. Korn (2007) Envelope syntheses of cylindrical vector-waves in 2-D random
 1110 elastic media based on the Markov approximation. *Earth, Planets, and Space* 59, 209-219.
- 1111 Schmerr, N. C., M. Banks, and Ingrid Justine Daubar. 2019. “The Seismic Signatures of
 1112 Recently Formed Impact Craters on Mars.” *Journal of Geophysical Research: Planets*,
 1113 1–19. <https://doi.org/10.1029/2019je006044>.
- 1114 Schmidt, R.M., Housen, K.R., 1987. Some recent advances in the scaling of impact and
 1115 explosion cratering. *International Journal of Impact Engineering, Hypervelocity Impact*
 1116 *Proceedings of the 1986 Symposium* 5, 543–560. [https://doi.org/10.1016/0734-](https://doi.org/10.1016/0734-743X(87)90069-8)
 1117 [743X\(87\)90069-8](https://doi.org/10.1016/0734-743X(87)90069-8)
- 1118 Shishkin, N.I., 2007. Seismic efficiency of a contact explosion and a high-velocity impact. *J.*
 1119 *Appl. Mech. Tech. Phys.* 48, 145–152. <https://doi.org/10.1007/s10808-007-0019-6>
- 1120 Smrekar, Suzanne E., Philippe Lognonné, Tilman Spohn, W. Bruce Banerdt, Doris Breuer,
 1121 Ulrich Christensen, Véronique Dehant, *et al.*, 2019. “Pre-Mission InSights on the Interior
 1122 of Mars.” *Space Science Reviews* 215 (1): 3. <https://doi.org/10.1007/s11214-018-0563-9>.
- 1123 Spiga, Aymeric, Don Banfield, Nicholas A. Teanby, François Forget, Antoine Lucas, Balthasar
 1124 Kenda, Jose Antonio Rodriguez Manfredi, *et al.*, 2018. “Atmospheric Science with
 1125 InSight.” *Space Science Reviews*. Springer Netherlands. [https://doi.org/10.1007/s11214-](https://doi.org/10.1007/s11214-018-0543-0)
 1126 [018-0543-0](https://doi.org/10.1007/s11214-018-0543-0).
- 1127 Stevanović, J., Teanby, N.A., Wookey, J., Selby, N., Daubar, I.J., Vaubaillon, J. and Garcia, R.,
 1128 2017. Bolide airbursts as a seismic source for the 2018 Mars InSight mission. *Space*
 1129 *Science Reviews*, 211(1-4), pp.525-545.
- 1130 Teanby, N. A., 2015. Predicted detection rates of regional-scale meteorite impacts on Mars with
 1131 the InSight short-period seismometer. *Icarus* 256, 49–62.

- 1132 Teanby, N.A., Wookey, J., 2011. Seismic detection of meteorite impacts on Mars. *Physics of the*
1133 *Earth and Planetary Interiors* 186, 70–80. <https://doi.org/10.1016/j.pepi.2011.03.004>
- 1134 Williams, J.P., Pathare, A.V., Aharonson, O., 2014. The production of small primary craters on
1135 Mars and the Moon. *Icarus* 235, 23–36.
- 1136 Wójcicka, N., Collins, G.S., Bastow, I.D., Teanby, N.A., Miljković, K., Rajšić, A., Daubar, I.,
1137 Lognonné, P., 2020. The seismic moment and seismic efficiency of small impacts on
1138 Mars. *JGR Planets*, submitted this issue.
- 1139

Figure 1.

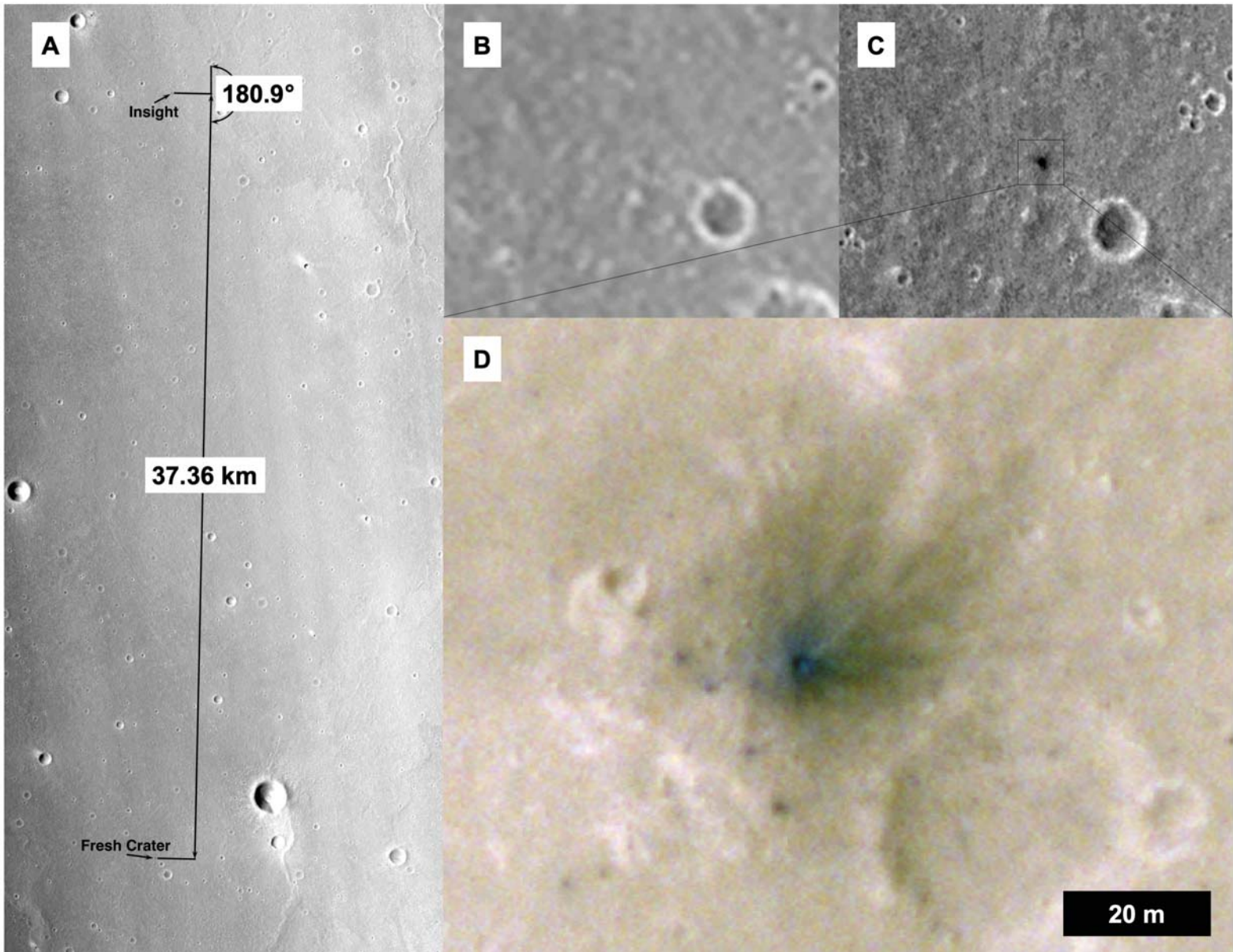


Figure 2.

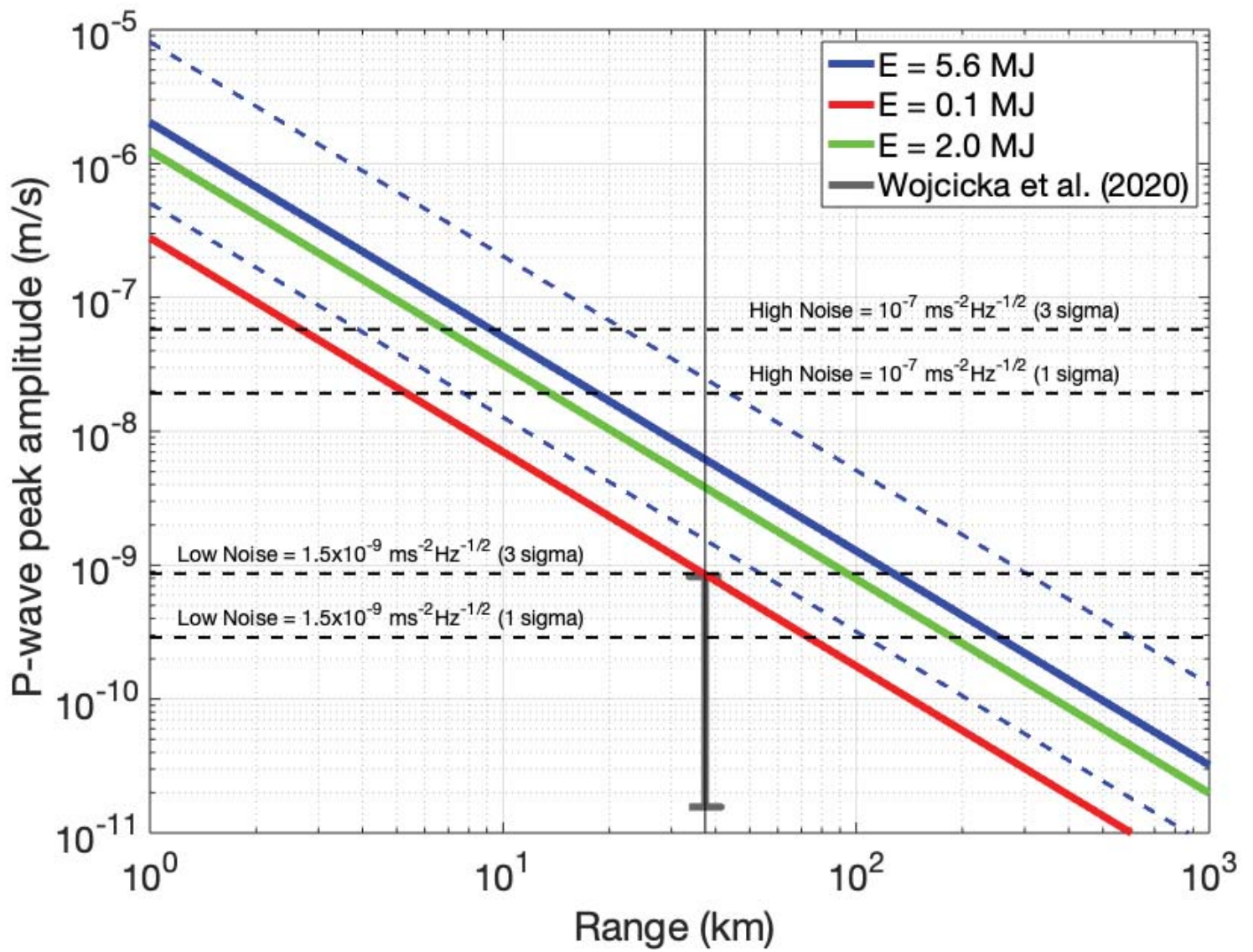


Figure 3.

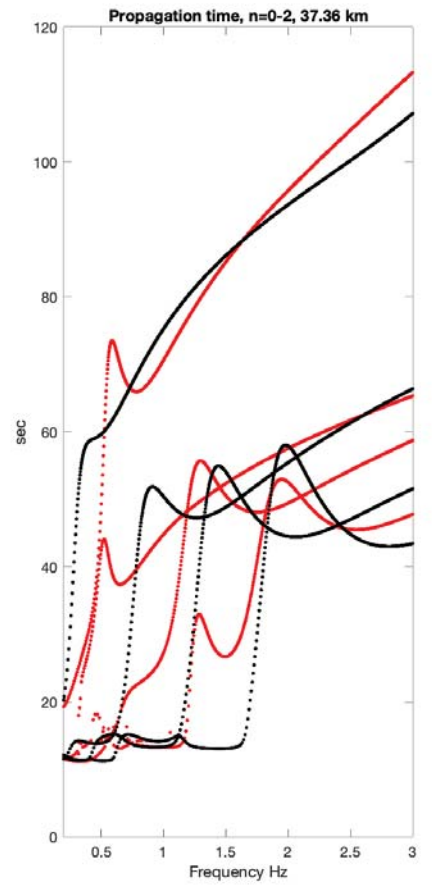
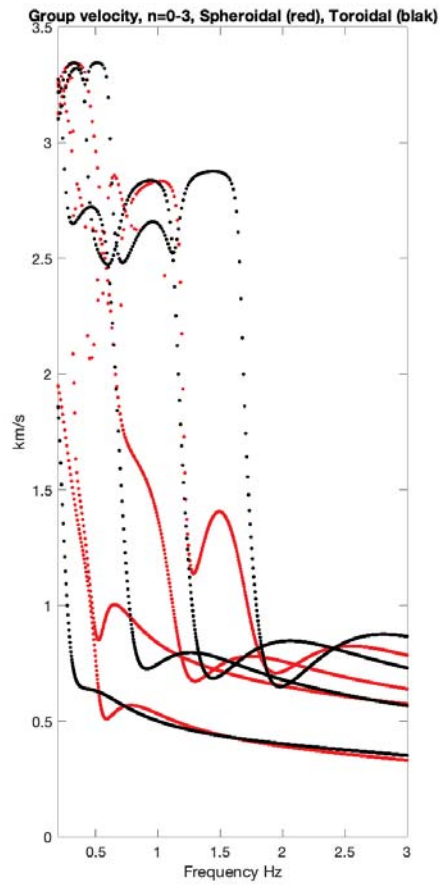
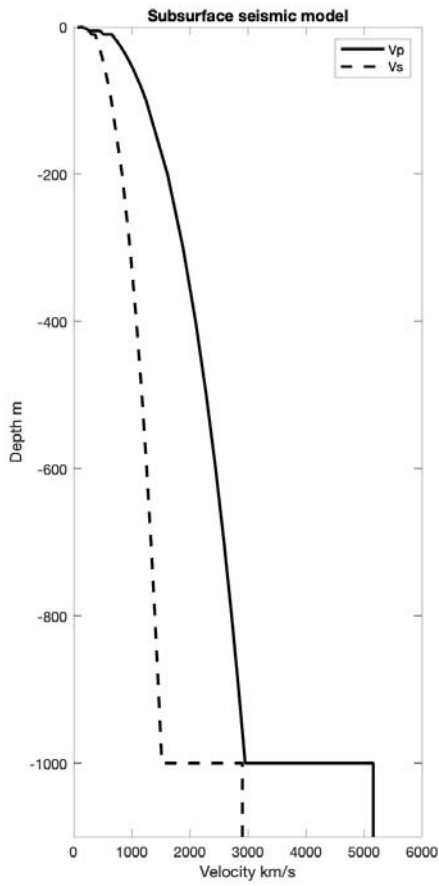


Figure 4.

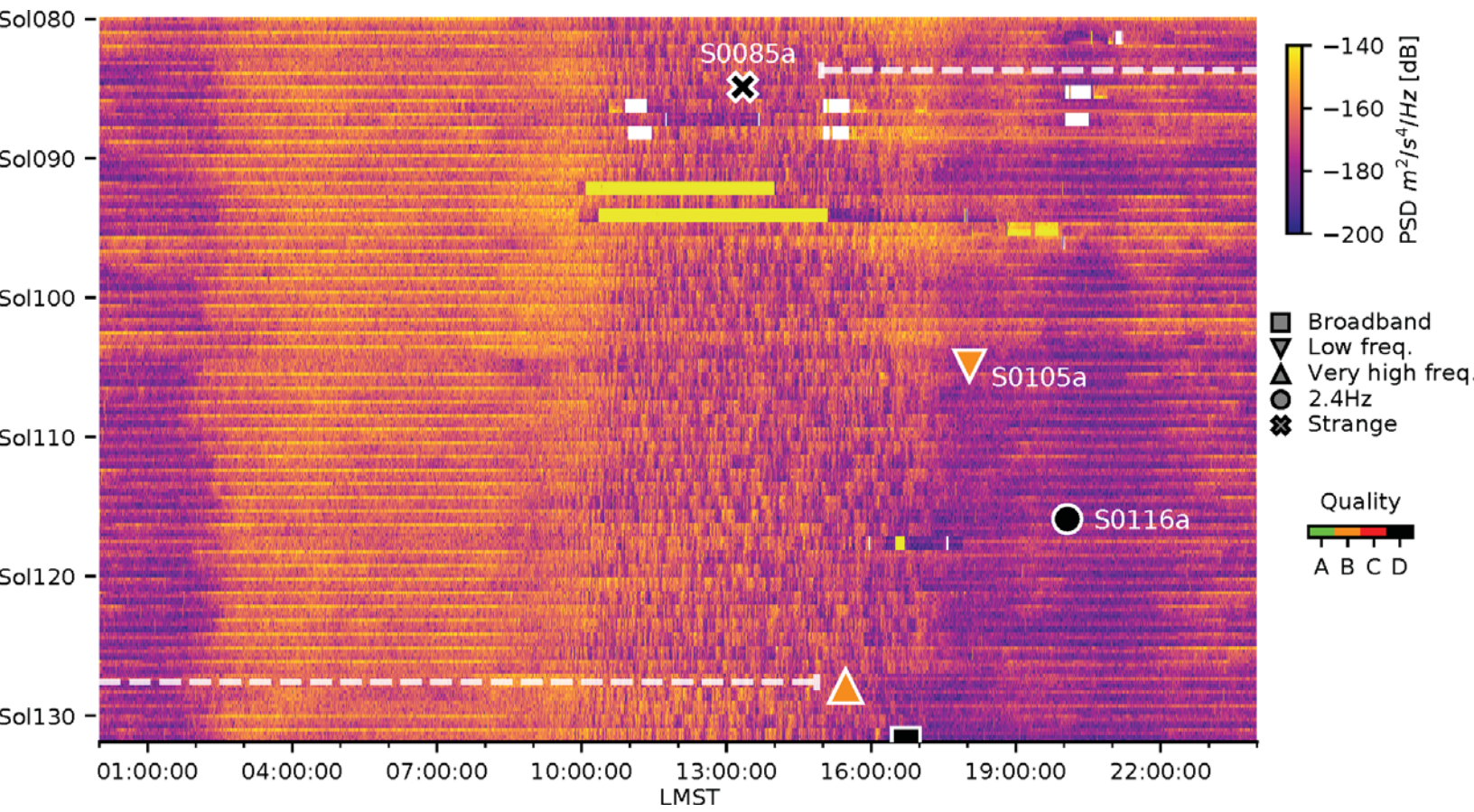


Figure 5.

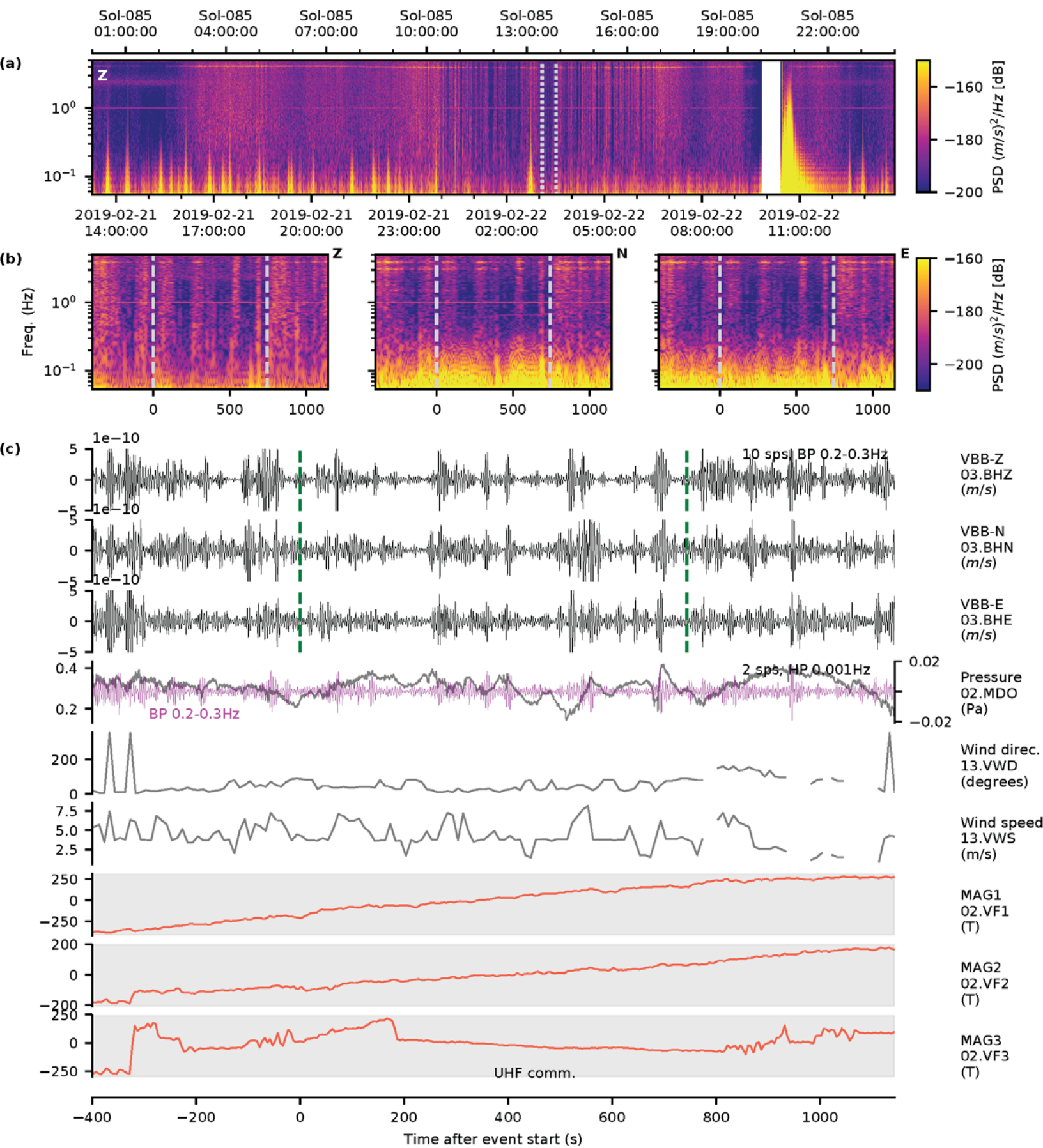


Figure 6.

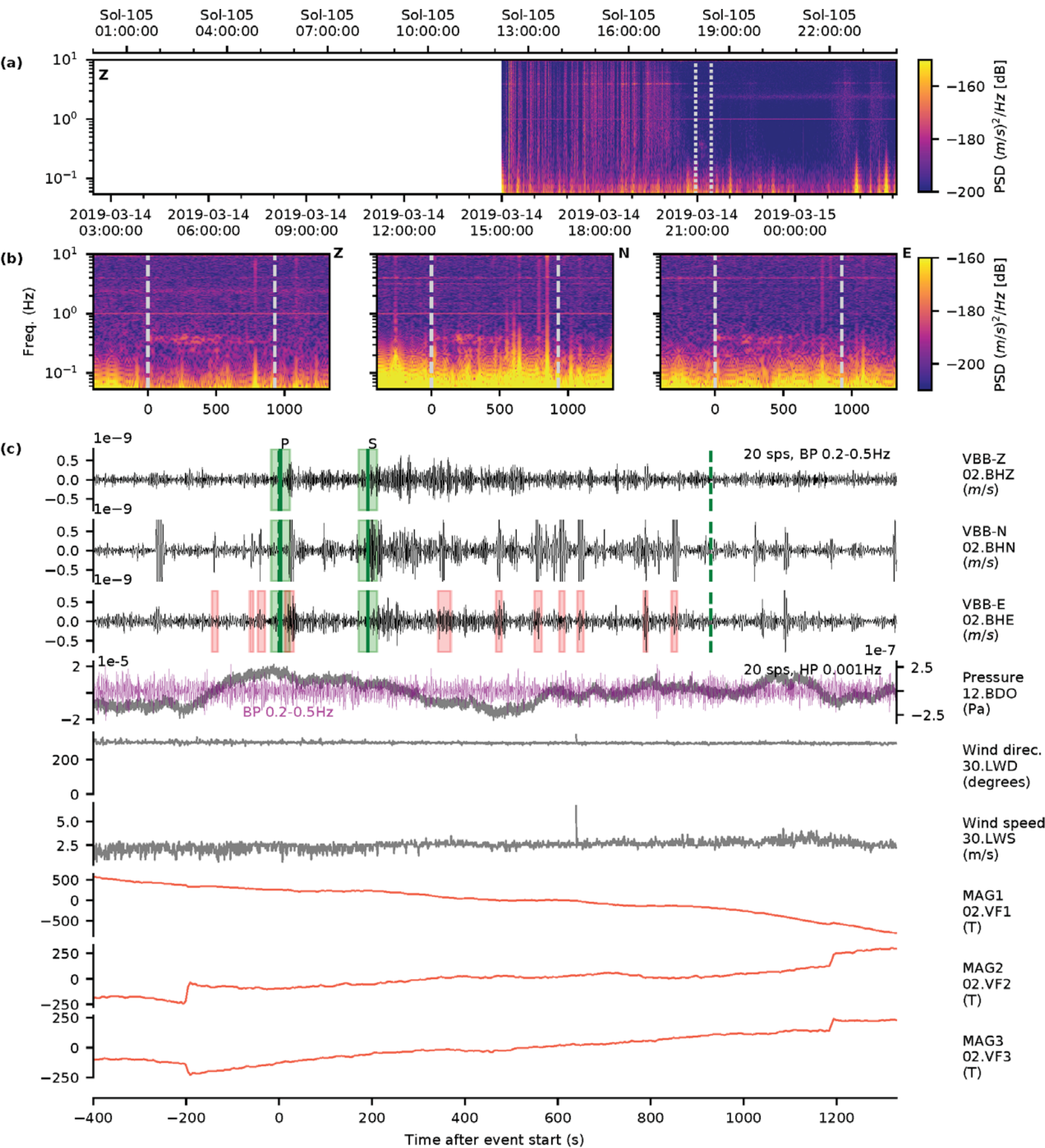


Figure 7.

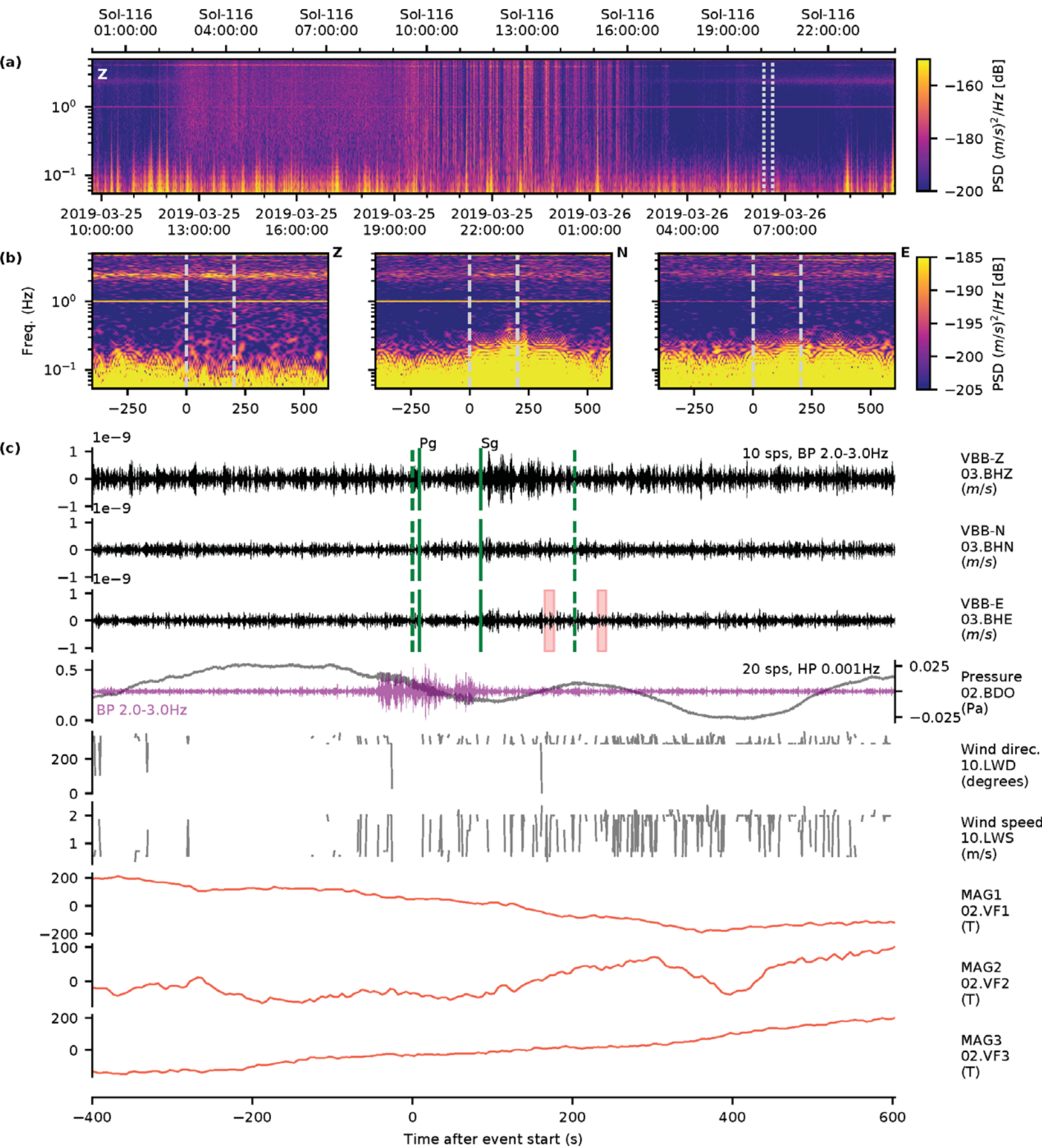


Figure 8.

Apollo 14 LM impact at LPZ12, LPZ14 and S0105 event on VBBZ

